Laboratory Landquakes: Insights From Experiments Into the High-Frequency Seismic Signal Generated by Geophysical Granular Flows

M. Arran, A. Mangeney, J. de Rosny, M. Farin, R. Toussaint, Olivier Roche

Laboratory landquakes: Insights from experiments into the high-frequency seismic signal generated by geophysical granular flows

M. I. Arran[1], A. Mangeney[1], J. De Rosny[2], M. Farin[2], R. Toussaint[3], O. Roche[4]

[1]Institut de Physique du Globe de Paris, CNRS (UMR 7154), Paris, France

[2]Institut Langevin, ESPCI Paris, PSL Research University, CNRS, Paris, France

[3]Institut de Physique du Globe de Strasbourg/EOST, University of Strasbourg, CNRS (UMR 7516), Strasbourg, France

[4]Université Clermont Auvergne, CNRS, IRD, OPGC, Laboratoire Magmas et Volcans, F-63000 Clermont-Ferrand, France.

Key Points:

- We conducted novel laboratory experiments to test five existing models for the high-frequency seismic signals generated by granular flows
- The 'thin-flow' model of Farin et al. (2019) was the most accurate and makes predictions consistent with empirical observations
- The ratio between the mean and fluctuating forces exerted by a granular flow varies greatly, determined by an inertial number of the flow

Corresponding author: Matthew Arran, `arran@ipgp.fr`

Abstract

Geophysical granular flows exert basal forces that generate seismic signals, which can be used to better monitor and model these severe natural hazards. A number of empirical relations and existing models link these signals' high-frequency components to a variety of flow properties, many of which are inaccessible by other analyses. However, the range of validity of the empirical relations remains unclear and the models lack validation, owing to the difficulty of adequately controlling and instrumenting field-scale flows. Here, we present laboratory experiments investigating the normal forces exerted on a basal plate by dense and partially dense flows of spherical glass particles. We measured the power spectra of these forces and inferred predictions for these power spectra from the models proposed by Kean et al. (2015), Lai et al. (2018), Farin et al. (2019), and Bachelet (2018), using Hertz theory to extend Farin et al. (2019)'s models to higher frequencies. The comparison of these predictions to our observations shows those of Farin et al. (2019)'s 'thin-flow' model to be the most accurate, so we examine explanations for this accuracy and discuss its implications for geophysical flows' seismic signals. We also consider the normalisation, by the mean force exerted by each flow, of the force's mean squared fluctuations, showing that this ratio varies by four orders of magnitude over our experiments, but is determined by a bulk inertial number of the flow.

Plain Language Summary

Landslides, like earthquakes, generate seismic signals: vibrations of the earth that can be detected a long way away. Analysis of the most rapid vibrations could provide information about how large a landslide is or how damaging it will be, helping emergency services respond. But full-size landslides are complex and difficult to study, so the generation of these vibrations is not yet sufficiently well understood for this information to be reliable. Therefore, in the place of full-size landslides, we studied simplified, small-scale versions in the laboratory, testing previous authors' predictions for the seismic signals they generate. We find that one set of predictions was particularly accurate and show that the corresponding predictions for full-size landslides are consistent with previous observations. This implies that a landslide's seismic signal can be used to calculate its size, its speed, and the typical size of particles within it.

1 Introduction

1.1 Background

Landslides and other geophysical granular flows are a major natural hazard, causing on average 4000 deaths worldwide each year from 2004 to 2016 (Froude & Petley, 2018) and an estimated billions of dollars of annual damage in the United States alone (Fleming et al., 1980; National Research Council, 1985; Schuster & Fleming, 1986). Many areas have little or no early warning system in place (Hervás, 2003; Guzzetti et al., 2020) and a damaging event's magnitude and effects may remain unknown for hours or days after it happens (Hervás, 2003; Scholl et al., 2017), hindering the response of emergency services and preventing those in a landslide's path from making even last-minute preparations. Modelling is currently unable to remedy these knowledge gaps, with poorly constrained parameters, such as a flow's basal friction coefficient, being important in determining a landslide's runout (van Asch et al., 2007; Lucas et al., 2014; Delannay et al., 2017; Cuomo, 2020).

Better monitoring of landslide-prone areas and better modelling of flows' evolution are therefore key to the reduction of landslide hazard, and the use of seismic signals is a promising tool towards these aims. Geophysical flows exert forces on the ground over which they travel, resulting in the outwards-propagating seismic waves that Kanamori and Given (1982) first described in detail, for an event at Mount Saint Helens. These seismic waves, which we refer to as 'landquakes', can be detected by a local or regional seismic network, permitting continuous monitoring of a wide area. This monitoring suggests the possibility of early warning systems, analogous to those in use and development for earthquakes (e.g. Given et al., 2018). Furthermore, landquakes encode information about a landslide's magnitude and evolution over time, and so these seismic signals can be analysed to assess damage, to constrain model parameters, and to compare different models.

The low-frequency components of landquakes encode the accelerations of a landslide's centre of mass, and initial work successfully analysed these components both to detect landslides and to reconstruct their trajectories. Authors first linked known landslides to signals in seismic data (e.g. Galitzine (Golitsyn), 1915; Jeffreys, 1923; Peterschmitt & de Visintini, 1964; Berrocal et al., 1978; Kanamori & Given, 1982; Hasegawa & Kanamori, 1987; Eissler & Kanamori, 1987; Weichert et al., 1994) before considering

–3–

theoretically the low-frequency signals generated by idealised landslides (e.g. Kawakatsu, 1989; Dahlen, 1993; Fukao, 1995). The theoretical framework of a single-force point source permitted the detection of landslides from seismic signals both locally (Lin et al., 2010; Chao et al., 2017) and globally (Ekström & Stark, 2013), while inversion for that force with single-block landslide models allowed their evolution to be reconstructed or their flow parameters to be constrained (Brodsky et al., 2003; La Rocca et al., 2004; Ekström & Stark, 2013; Allstadt, 2013; Yamada et al., 2013; Coe et al., 2016). Other authors (e.g. Favreau et al., 2010; Moretti et al., 2012, 2015, 2020; Yamada et al., 2016, 2018; Zhao et al., 2020) used a higher-order approximation towards the same aim, simulating landslides as continuous mass distributions rather than point masses and calculating the corresponding low-frequency synthetic landquakes. Comparison to observed seismic signals then permitted higher-resolution reconstruction of mass releases and flow trajectories, and the estimation of spatially varying flow parameters. However, such low-frequency seismic waves can only be detected for large landslides and, even if detected, cannot provide information on many properties relevant to landslide modelling and harm assessment, such as the size of individual particles within the flow or the vertical profiles of flow properties.

To extract more information and infer these properties, previous authors suggest using the high-frequency component of landquakes, associated with the accelerations of individual particles within the flow. The spectrogram of this high-frequency component and its envelope have distinctive shapes (Suriñach et al., 2005) which can be used to detect landslides (Hibert et al., 2014; Dammeier et al., 2016; Fuchs et al., 2018; Lee et al., 2019). Furthermore, the properties of this envelope can be related to those of the landslide: the envelope's duration to the landslide's duration and hence its loss of potential energy (Deparis et al., 2008; Hibert et al., 2011; Levy et al., 2015); the envelope's amplitude to the seismic energy emitted by the landslide and hence its volume (Norris, 1994; Hibert et al., 2011; Levy et al., 2015), its work rate against friction (Schneider et al., 2010; Levy et al., 2015), and its momentum (Hibert et al., 2015, 2017); and envelope scale and shape parameters to the landslide's geometry via multilinear regression (Dammeier et al., 2011). Without a theoretical framework for the high-frequency component of landquakes, however, both the precision and the range of validity of these relations are unclear, and it is difficult to use them to assess a landslide's damage or to better predict it. A model for landquake generation is required.

1.2 Existing Models

Models of the high-frequency component of landquakes rely on the same framework: consideration of the total seismic signal as a sum of the uncorrelated signals generated by individual, random particle impacts, with the properties of the impacts determined by some mean properties of the particulate flow and with a specified Green's function mapping the force of an individual impact to the seismic signal observed at a remote station. This stochastic impact framework arises from Tsai et al. (2012)'s model of seismic noise generation from riverine sediment transport, and we discuss its validity in S2. We expect that it will be applicable to any extensive flows of stiff particles for which energetic impacts are more significant than other high-frequency sources, for signal periods smaller than the timescales over which the bulk flow varies. Examples may include avalanches, debris flows, and rockfalls involving multiple blocks.

Assuming the framework's validity, prediction of a flow's high-frequency landquake signal requires consideration of the locations $\mathbf{x} \in V$ of signal generation, and the specification of just three things at each location: 1) the number $n_I(\mathbf{x})$ of impacts per unit volume and time; 2) the force $\mathbf{F}_I(\mathbf{x}, t)$ applied by a single, typical impact over its duration; and 3) the Green's function $\mathbf{G}(t, \mathbf{r}; \mathbf{x})$ for the scalar velocity response $v_{\mathbf{r}}(t)$ to that force of the seismic station detecting the signal, located at $\mathbf{r}$. Writing $\tilde{\cdot}$ for Fourier transforms over time Δt, the landquake signal will then have power spectral density

$$P_{v_{\mathbf{r}}}(f) = |\tilde{v}_{\mathbf{r}}(f)|^2 / \Delta t = \int_V n_I(\mathbf{x}) |\tilde{\mathbf{F}}_I(\mathbf{x}, f) \cdot \tilde{\mathbf{G}}(f, \mathbf{r}; \mathbf{x})|^2 \, d\mathbf{x}. \tag{1}$$

1.2.1 Direct Use of Tsai et al. (2012)

Kean et al. (2015), Lai et al. (2018), and Farin et al. (2019) consider only impacts on exposed bedrock at the base of a flow to be significant in signal generation, and assume 1) that the rate of impacts is determined by the advection of particles, with the mean flow, into basal irregularities of the same scale; 2) that the force a particle exerts varies over timescales much shorter than the range of periods to which the seismic station is sensitive; and 3) that the relevant Green's function is that for Rayleigh-wave propagation to the far field. Under these assumptions, if a representative impacting particle has diameter d and downslope speed u, it will have collision rate u/d, so that a bedrock-contacting flow area A in which impacting particles have a volume fraction ϕ will have an approximate integrated collision rate $\int_V n_I \, d\mathbf{x} = \phi A u / d^3$. For all signal periods of

–5–

145   interest, the typical force applied by an impact will be approximable as a Dirac delta func-

146   tion in time and hence constant in the frequency domain, equal to the impulse transferred,

147   so that we may write $\tilde{\mathbf{F}}_I(f) = \Delta p \mathbf{e}_I$ for a unit vector $\mathbf{e}_I$ in the direction of the impulse.

148   Meanwhile, the relevant frequency-space Green's function for a station at radius r will

149   have magnitude $|\mathbf{e}_I \cdot \tilde{\mathbf{G}}| = R(f)e^{-\alpha(f)r}/\sqrt{r}$, for functions R and α related to Rayleigh-

150   wave propagation and inelastic attenuation, respectively. Consequently, the signal's power

151   spectral density is

$$P_{v_{\mathbf{r}}}(f) = \frac{\phi A u \Delta p^2}{d^3 r} R(f)^2 e^{-2\alpha(f)r}. \tag{2}$$

153   Kean et al. (2015) suggests that u scales with the measured surface velocity and

154   Δp with the base-normal component of the flow's local weight per unit area. The au-

155   thors use an empirical, piecewise-continuous function α, and avoid consideration of scal-

156   ing constants, ϕ, R and d by examining only the ratio of $P_{v_{\mathbf{r}}}(f)$ to that measured dur-

157   ing a reference debris flow in the same channel, for which such parameters are assumed

158   to be the same. The paper uses this model to estimate the depths of static sediment 'shield-

159   ing' the channel centre from impacts, and these estimates correctly remain positive, but

160   the paper performs no further evaluation of the model.

161   Lai et al. (2018) suggests that large, flow-depth-spanning particles dominate the

162   signal, so that d should be the 94th percentile of the particle diameter distribution and

163   u should be the depth-averaged downslope velocity $\bar{u}$ of the flow. The authors implic-

164   itly take $\phi = 1$ and further assume that impacts transfer an impulse equal to that for

165   elastic rebounds of individual near-spherical particles at vertical velocity $\bar{u}$, such that

166    $\Delta p = \pi \rho d^3 \bar{u}/3$ for particle material density ρ. Equations for $R(f)$ and $\alpha(f)$ are taken

167   from Tsai et al. (2012), Tsai and Atiganyanun (2014), and Gimbert and Tsai (2015), and

168   then applied to a Californian debris flow, to invert the peak frequency of $P_{v_{\mathbf{r}}}(f)$ for r.

169   However, this inversion relies on the model for signal generation only via the assump-

170   tion that $|\tilde{\mathbf{F}}_I(f)|$ is independent of f in the frequency range of interest, so this assump-

171   tion is the only part of the model that the paper tests.

172   Farin et al. (2019) generalises the model of Lai et al. (2018) to different flow regions

173   and regimes and to a continuous particle size distribution. The authors calculate that

174   the impacts of particles falling from the flow front or saltating ahead of it are less sig-

175   nificant for signal generation than those in the flow's dense snout and body. In these two

176   regions, for 'thin' flows of depth h comparable to the largest particle diameters, the pa-

per suggests that the Lai et al. (2018) model will hold, with slight modifications: ϕ is explicitly stated; there are extra terms in the equation for Δp to account for inelasticity and variation in the angle and velocity of impacts; R is adjusted to account for non-vertical $\mathbf{e}_I$; and d is represented by its appropriately weighted average over the distribution of particle diameters, which is suggested to be approximately equal to the 73rd percentile of that distribution. However, for 'thick' flows, where h is much larger than the particles' diameters, the paper suggests that, in addition to the above slight modifications, the relevant advection and impact velocity is that of base-adjacent particles. Assuming no basal slip, in the sense that velocities tend to zero towards the flow's base, u is then proportional to $\bar{u}d/h$ and the representative value of d is equal to the 86th percentile of the particle diameter distribution. The authors tested neither of the 'thin-flow' and 'thick-flow' models.

1.2.2 Model of Bachelet (2018)

In contrast to the above papers, Bachelet (2018) considers impacts between different layers of particles, throughout the depth of the flow, and supposes 1) that the local impact rate is the rate at which adjacent layers shear over each other; 2) that the force throughout an impact is described by Hertz theory with typical impact velocity equal to the standard deviation in particle velocity within each layer; and 3) that the Green's function includes exponential attenuation of the force with the impact's distance from the flow's base.

The use of Hertz theory to describe the contact force between impacting particles, detailed in S3, predicts the duration of impacts and so a frequency scale for the spectral density of the forces they exert. For a collision at relative normal velocity u_n between two spherical particles of diameter d, consisting of material with density ρ, Young's modulus E, and Poisson's ratio ν, Hertz theory predicts a timescale for the impact

$$\tau = \left[\frac{\pi^2 \rho^2 (1-\nu^2)^2}{4E^2 u_n} \right]^{1/5} d. \tag{3}$$

With this τ, the spectral density of the normal force between the particles is

$$|\tilde{F}_I(f)|^2 = \left(\frac{\pi \rho d^3 u_n}{3} \right)^2 \zeta(f\tau) \tag{4}$$

for a non-dimensional function $\zeta(f\tau)$, plotted in S3, which is approximately equal to 1 for $f\tau \ll 1$, monotonically decreases to $\zeta(f\tau) = 0.5$ for non-dimensional corner fre-

207   quency $f_c\tau \approx 0.208$, and is much less than 1 for $f\tau > 1$. Impacts at higher velocities

208   u_n apply forces with higher spectral density, over a wider frequency range.

209   This spectral density doesn't appear explicitly in Bachelet (2018), which instead

210   uses the integral of ζ over all $f\tau$ to consider the total seismic power generated by a flow.

211   However, we can follow the thesis' reasoning to derive from equation (4) a prediction for

212   the spectral density of a flow's high-frequency landquake signal, in the form of equation

213   (1). First, separating a flow with representative particle size d and particle volume frac-

214   tion ϕ into layers, and writing z_j for the vertical position of each layer and u_j for the mean

215   horizontal velocity within it, the thesis suggests that the rate of impacts is

$$n_I(\mathbf{x}) = \frac{4\phi}{\pi d^3}\sum_j (u_j - u_{j-1})\delta(z - z_j) \qquad (5)$$

217   for Dirac delta function δ. Then, writing T_j for the granular temperature in the jth layer,

218   equal to the variance of individual particles' velocities, the thesis takes the spectral den-

219   sity of the force applied by a typical impact to be given by equation (4) with impact ve-

220   locity $u_n = \sqrt{T_j}$. Finally, the magnitude of the frequency-space Green's function for

221   an impact at height z is taken to be $e^{-\gamma z/2}|\tilde{G}_b|$, where γ is an attenuation constant and

222    $|\tilde{G}_b|$, describing a measurement station's velocity response to vertical basal forces, is con-

223   stant due to the assumption of an incoherent, diffuse seismic field with constant atten-

224   uation. Therefore, a flow of area A will generate a landquake signal with power spectral

225   density

$$P_{v_r}(f) = \frac{4\phi A}{\pi d^3}|\tilde{G}_b|^2\sum_j (u_j - u_{j-1})\Delta p_j^2\zeta(f\tau_j)e^{-\gamma z_i} \qquad (6)$$

227   for

$$\Delta p_j = \frac{\pi\rho d^3\sqrt{T_j}}{3}, \quad \tau_j = \left[\frac{\pi^2\rho^2(1-\nu^2)^2}{4E^2\sqrt{T_j}}\right]^{1/5} d. \qquad (7)$$

229   Bachelet (2018) shows this model to be consistent with measurements of the seis-

230   mic signals generated by approximately steady and uniform laboratory-scale granular

231   flows, but the results are not conclusive. Releasing flows of $d = 2\,\text{mm}$-diameter glass

232   beads in a channel inclined at angles between $16.5°$ and $18.1°$, accelerometers were used

233   to estimate the total seismic power imparted to an isolated plate by overlying flows of

234   depths between $15d$ and $20d$, and this power was compared to the prediction of equa-

235   tion (6), with flow parameters estimated using high-speed photography through the chan-

236   nel's transparent sidewalls. The agreement is reasonable, but is highly dependent on the

237   fitted parameter γ, and so the number of estimates, and their range of variation, are too

238 small for conclusions to be definitive. The use of Hertz theory permits predictions for

239 the frequency-dependence of the power spectral density, but no such predictions are com-

240 pared with experimental results. Further tests are therefore required.

1.3 Aim of This Paper

242 This paper aims to test the above models of high-frequency landquake signal gen-

243 eration. Studying a range of granular flows and measuring the parameters used by the

244 above models, we aim to compare observed landquake signals to the models' predictions.

245 Because we are concerned with the generation of the signal, rather than its propagation,

246 we consider predictions for the power spectral density P_F of the total base-normal force

247 exerted by the flow, which may be obtained by removing the Green's function in equa-

248 tion (1), so by dividing equation (2) by $R^2 e^{-2\alpha r}/r$ and equation (6) by $|\tilde{G}_b|^2$. P_F will

249 be proportional to the spectral density of the signal at a receiver, with its appropriately

250 weighted integral proportional to the seismic power transmitted by the flow, but P_F, un-

251 like these measurements, is independent of the response of the base on which the flow

252 propagates.

253 However, it is difficult to use field-scale granular flows to test the models' predic-

254 tions for P_F. Natural geophysical flows often occur in remote locations, infrequently and

255 unpredictably, and so the sites of most flows are not instrumented for measurements of

256 flow parameters. Where sites are instrumented, the destructiveness of geophysical flows

257 restricts which parameters can be measured, excluding most used by the above models.

258 Furthermore, geophysical flows are typically extremely unsteady and heterogeneous, so

259 that any given landquake signal may be produced by a flow region with parameters very

260 different from those that have been measured. Finally, the inference from a landquake

261 signal of the forces that generated it requires inversion of the Green's function, which

262 is typically poorly constrained at the high frequencies of interest, and to which the in-

263 version is typically very sensitive at precisely these high frequencies.

264 We therefore conducted laboratory experiments to link the properties of a gran-

265 ular flow to the seismic signal it generates. In the laboratory, flows can be fully controlled

266 and instrumented, allowing a wide range of parameter values to be explored and mea-

267 sured. Apparatus can be designed to produce steady, uniform, homogeneous flows, and

268 the Green's function can be well constrained over a large frequency range by calibration.

269 Having established the relevant physics, conclusions drawn from laboratory results can

270 then be scaled up to describe field-scale flows.

2 Methods

2.1 Experimental Apparatus

273 As the simplest possible analogue of a geophysical granular flow, we studied the

274 flow of spherical glass beads, $d = 2\,\text{mm}$ in diameter, in an inclined channel $2.5\,\text{m}$ long

275 and $W = 0.2\,\text{m}$ wide, shown in Figure 1. The beads were 1.7-2.1 mm Type S glass beads

276 produced by Sigmund Lindner GmbH and provided by MINERALEX, with material den-

277 sity $\rho = 2500\,\text{kg}\,\text{m}^{-3}$ and Young's modulus $E = 63$ GPa (Sigmund Lindner, 2018).

278 In each experiment, $40\,\text{kg}$ of beads were initially stored in a plastic reservoir of volume

279 $0.08\,\text{m}^3$, from which they flowed out via a rectangular opening of width $0.18\,\text{m}$ and ad-

280 justable height h_g, controlled to within $0.06\,\text{mm}$ by a plastic gate which was fixed in place

281 during each experiment. A separate plastic release gate blocked this opening before each

282 experiment and was manually lifted to start outflow. On leaving the reservoir, beads en-

283 tered the separately supported channel, which had an aluminium base; transparent, 0.1 m-

284 high acrylic walls; and an incline $\tan\theta$, which could be adjusted by changing the heights

285 of the braces attaching the channel to its supports. The channel's base was roughened

286 with the same type of glass beads as constituted the flow, fixed in place with extra-strong

287 double-sided carpet tape, with an irregular, dense pattern achieved by random pouring.

288 The flow of beads down the channel adjusted to these conditions over a distance

289 of $1.92\,\text{m}$, before reaching a rectangular, instrumented steel plate set into a correspond-

290 ing hole in the centre of the channel's base. The plate was $X = 0.18\,\text{m}$ long, $Y = 0.1\,\text{m}$

291 wide, and $H = 2\,\text{mm}$ thick, with its surface flush with that of the aluminium base to

292 within $0.02\,\text{mm}$ and separated from it by an isolation gap of $0.04\pm0.01\,\text{mm}$, achieved

293 by using strips of plastic film as spacers during emplacement. The plate was supported

294 by a force sensor and a support piece, with the three separated by washers and held to-

295 gether by a prestressing screw, the head of which was glued into a $0.5\,\text{mm}$-deep recess

296 in the centre of the plate's underside. The support piece, in turn, was attached to the

297 channel's substructure using phenyl salicyclate (salol), which was added to the join when

298 molten and solidifed to form a stiff connection, but could be melted with a heat gun for

299 removal of the plate or adjustment of its position. Before the plate's emplacement, we

used the same salol to roughen its surface with glass beads: heating the plate, we added salol to form a thin, liquid layer, and we poured beads on top to form an irregular, dense pattern, before the salol solidified and fixed them in place.

After the plate, the flow of beads continued for $0.4\,\mathrm{m}$, before flowing out of the channel and into a plastic outflow tray. Plastic sheeting extended the tray's walls, to prevent energetic particles from escaping.
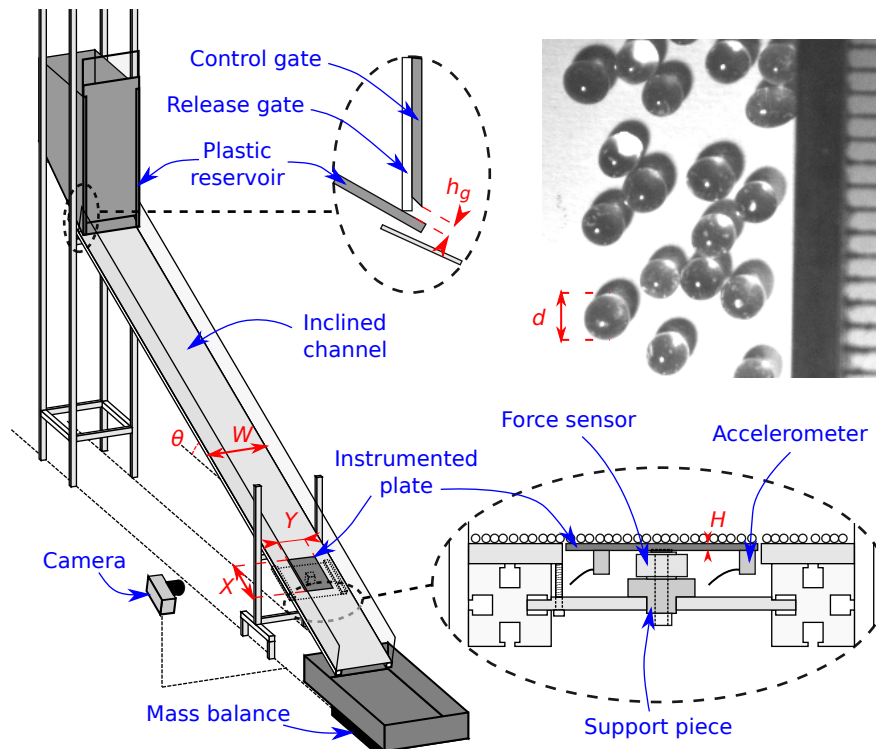
Figure 1. *Schematic of experimental apparatus.* Experiments are conducted in the channel represented, to scale, at left, with components of the apparatus labelled in blue and relevant dimensions in red. Expansions at top-centre and bottom-right represent, in cutaway views and not to scale, details of the reservoir and the instrumented plate, respectively. The glass beads used in experiments are shown at top-right, with a mm-unit scale.

Four sets of devices took measurements of the flow: a mass balance beneath the outflow tray; the force sensor supporting the instrumented plate; four accelerometers attached to the plate's underside; and a high-speed camera directed through the channel's wall. The mass balance was a Dymo S50 digital shipping scale, which measured in each experiment the cumulative mass that had passed through the channel. The force sen-

311   sor was a Kistler 9027C three-component force sensor and was connected to a Kistler

312   5073 charge amplifier, measuring the normal, downslope, and cross-slope forces exerted

313   by the flow on the plate. The accelerometers were Brüel and Kjær type 8309 accelerom-

314   eters, attached with salol to randomly selected positions on the plate's underside and

315   connected to a Brüel and Kjær Nexus 2692-A-OS4 conditioning amplifier, to measure

316   the normal vibrations of the plate and hence the seismic energy imparted to it by the

317   flow. Settings of the force sensor and accelerometer amplifiers are described in S4. The

318   camera was an Optronis CR600x2, with a Sigma 17-50 mm F2.8 EX DC lense, and was

319   level with and focussed on the inside of the channel sidewall, directly cross-slope from

320   the instrumented plate's centre. The camera's inclination was the same as the channel's

321   and its field of view was 640x256 pixels, corresponding to a region $8\,\mathrm{cm}$ long and $3.2\,\mathrm{cm}$

322   high. The sidewall was lit using a Photonlines H5 LED light, via a white sheet of pa-

323   per which acted as a reflective diffuser, and we used an exposure of $250\,\mathrm{\mu s}$ and a frame

324   rate of $2000\,\mathrm{s}^{-1}$.

325   To control the measurement devices, we used an Arduino Uno R3 microcontroller

326   board, and we recorded measurements using a Pico Technology Picoscope 4824 oscillo-

327   scope connected to a Lenovo E530 laptop. Measurements from the mass balance, force

328   sensor, and accelerometers were recorded from the time $t = 0$ at which the reservoir's

329   release gate was lifted until the outflow stopped at $t = t_e$, while the camera recorded

330   footage over a duration Δt_c between $2\,\mathrm{s}$ and $10\,\mathrm{s}$, after a delay time t_d in which the flow

331   developed into a steady state. Details are in S5.

332   We conducted experiments with six different channel inclinations between $22.8°$ and

333    $27.5°$ ($\tan\theta = 0.42, 0.44, 0.46, 0.48, 0.50$ and 0.52), with this order randomised to negate

334   the effect of any systematic variation in atmospheric conditions or measurement sensi-

335   tivity. For each inclination, we conducted three repeats with the reservoir control gate

336   at each of four different heights ($h_g = 5\,\mathrm{mm}, 10\,\mathrm{mm}, 20\,\mathrm{mm}$ and $40\,\mathrm{mm}$), with the or-

337   der of gate heights again selected at random.

338   At channel inclines equal to and greater than $\tan\theta = 0.46$ ($\theta = 24.7°$), there was

339   a gate height below which flows were in the gaseous regime of e.g. Börzsönyi and Ecke

340   (2006) and Taberlet et al. (2007), with all glass beads in saltation and accelerating downs-

341   lope. We recorded no measurements of such flows, which were energetic and far from sta-

342   tionary, with a large number of beads escaping across the channel's sidewalls and with
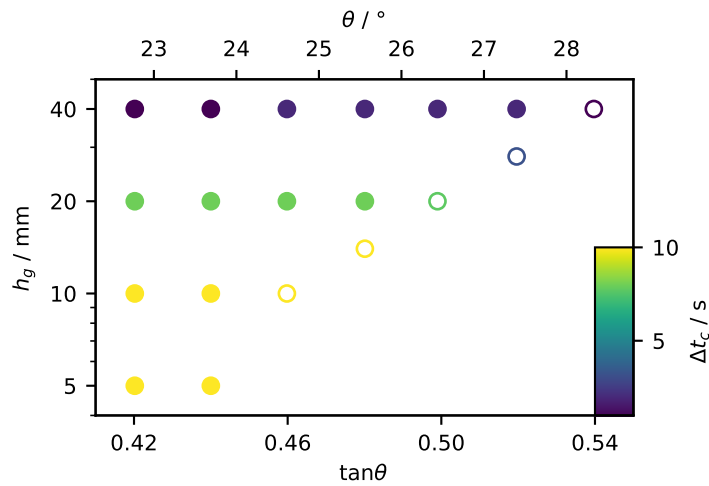
Figure 2. *Channel inclines* $\tan\theta$ *and release gate heights* h_g *used in experiments.* ○ indicates an experiment for which the flow was in the transitional regime, while colours indicate the duration of time Δt_c recorded by the camera.

the camera's images unusable for reliable measurements. At each such incline, we instead recorded measurements at all gate heights resulting in dense flows and at one gate height resulting in a 'transitional-regime' flow, with a dense basal flow below a saltating layer. These gate heights are plotted in Figure 2, within the full parameter space investigated.

2.2 Data Analysis

For each experiment within the parameter space, we analysed the experimental data to calculate dynamic, seismic, and kinematic properties of the flow: the mass of particles that lay over the instrumented plate and the effective friction coefficient between the two; the mass flux of particles through the channel and their average velocity; the power spectrum of the normal force exerted on the plate by the flow; and the vertical profiles of particle volume fraction, velocity, and granular temperature at a channel wall. We recall that W denotes the channel's width and θ its angle of inclination; that X, Y, and H denote the length, width, and thickness of the plate; and that t_d and Δt_c denote the delay before and the duration of the high-speed camera's recording, respectively. These and all other variables are listed in S1 and all code used to perform these analyses is available at Arran et al. (2020).

To infer the mass overlying the plate and its effective friction coefficient with the flow, we used the data from the force sensor. Averaging over successive 0.5 ms intervals, the net downslope force $F_x(t)$ and plate-normal, downwards force $F_z(t)$ applied to the plate by the flow were calculated from the voltage output of the force sensor's charge amplifier, as described in S6. Then, assuming no net plate-normal acceleration of the flow overlying the plate, over the period of steady flow recorded by the camera, we calculated the average mass per unit area overlying the plate as

$$\sigma = \frac{\langle F_z \rangle_{\Delta t_c}}{XY g \cos \theta}, \tag{8}$$

where $\langle \cdot \rangle_{\Delta t_c}$ represents the arithmetic mean over $t_d < t < t_d + \Delta t_c$ and g represents gravitational acceleration. Similarly, we followed Hungr and Morgenstern (1984) and Roche et al. (2020) in calculating the effective friction coefficient as

$$\mu = \frac{\langle F_x \rangle_{\Delta t_c}}{\langle F_z \rangle_{\Delta t_c}}, \tag{9}$$

with this calculation validated in S6, section S6.3.

To calculate the mass flux through the channel, we examined the data recorded by the mass balance. Having the cumulative mass $M(t)$ that had flowed through the channel after time t, we calculated the average flux per unit channel width, over the period of steady flow recorded by the camera, as

$$q = \frac{M(t_d + \Delta t_c) - M(t_d)}{\Delta t_c W}. \tag{10}$$

Assuming this average mass flux to be equal to that across the plate, and having calculated the mass overlying the plate, we could then calculate the mean depth-averaged flow velocity across the plate,

$$\bar{u} = q/\sigma. \tag{11}$$

To extract the power spectral density of the flow's basal force, we processed data from the accelerometers using Kirchhoff-Love plate theory and assuming perfect isolation of the plate from the channel and linear attenuation within the plate. On the basis of the steel's technical documentation (John Steel, 2019; Steel SS, 2019), we took its density to be $\rho_p = 7800 \, \text{kg m}^{-3}$, its Young's modulus to be $E_p = 200 \, \text{GPa}$, and its Poisson's ratio to be $\nu_p = 0.29$. Then, its bending stiffness was $D = E_p H^3 / 12(1 - \nu_p^2)$ and the mean bandgap between its resonant frequencies was $\Delta_f = 2\sqrt{D}/XY \sqrt{\rho_p H} \approx 400 \, \text{Hz}$.

Assuming that the spectral density of an impact's force varied little over this frequency scale, this spectral density was estimated using D, the proportion of the plate's energy $\mathcal{P}$ in its steel structure's vertical displacements, the quality factor Q describing the attenuation of energy in the plate, and the accelerations $a_j(t)$ measured by the four accelerometers, as

$$P_F(f) = \frac{|\tilde{F}(f)|^2}{\Delta t} \approx \frac{(\rho_p H)^{3/2} XY\sqrt{D}}{\pi \mathcal{P} Q f \Delta t} \langle \sum_{j=1}^{4} |\tilde{a}_j(f)|^2 \rangle_{\Delta f}, \tag{12}$$

where Fourier transforms are over a time interval $\Delta t = 0.2\,\text{s}$, and $\langle \cdot \rangle_{\Delta f}$ represents a moving average over frequency, with window width $\Delta f = 2\,\text{kHz}$. We describe in S7, section S7.1 the derivation of this relation and the calculation of $|\tilde{a}_j|^2$ from the voltage output of the accelerometers' conditioning amplifer; in section S7.2 the calibration we performed to measure the plate parameters $\mathcal{P} = 0.25$ and $Q = 99$ and to extend the flat frequency range of the accelerometers to $120\,\text{kHz}$; and in section S7.3 the validation of this work.

Finally, to extract profiles of kinematic properties at the channel wall, we analysed the images taken by the high-speed camera, using particle tracking velocimetry and Gaussian coarse-graining. Analysing each frame in turn, we detected the positions (x_j, z_j) of particles at the channel walls and, tracking particles between consecutive frames, calculated their mean velocities over each $0.5\,\text{ms}$ interval. Calculating the smoothed velocities $\mathbf{u}_j$ over five frames, or $2.5\,\text{ms}$, we estimated the downslope-averaged and time-averaged base-normal profiles at the channel's wall of relative volume fraction $\phi_w(z)$, mean velocity $\mathbf{u}_w(z)$, and granular temperature $T_w(z)$ as

$$\phi_w(z) = \langle \sum_j C(z_j; z)\pi d^2/4 \rangle_{\Delta t_c}, \tag{13}$$

$$\mathbf{u}_w(z) = \langle \sum_j C(z_j; z)\pi d^2 \mathbf{u}_j/4 \rangle_{\Delta t_c}/\phi_w(z), \tag{14}$$

$$T_w(z) = \langle \sum_j C(z_j; z)\pi d^2 ||\mathbf{u}_j - \mathbf{u}_w(z)||^2/4 \rangle_{\Delta t_c}/\phi_w(z), \tag{15}$$

where averages are over all frames recorded by the camera, sums are over all particles tracked in each frame, and the coarse-graining function C is localised around z, with integral over the total spatial domain equal to 1. This process is described in detail in S8.

While the irregularity of the flow's base and surface complicate the definition of the flow thickness h, we take the base-normal co-ordinate z to be zero at the top of the

base's fixed beads, and extract h as the value of z at which $\phi_w(z)$ drops below half its maximum value,

$$h = \min\{z > \text{argmax } \phi_w | \phi_w(z) < \max(\phi_w)/2\}. \tag{16}$$

For a flow with constant particle volume fraction below a level surface, this exactly corresponds to the intuitive flow depth. Whilst other reasonable definitions lead to different specific results, they do not alter our conclusions.

2.3 Model Predictions

For each of the models described in section 1.2, for a granular flow's seismic signal, we inferred predictions for the experimental seismic signal. Specifically, we expressed a prediction $\hat{P}_F$ for the power spectrum of the base-normal force applied by the flow to the instrumented plate, as a function of the flow properties specified in section 2.2: the mean depth-averaged flow velocity $\bar{u}$, the mass overburden per unit area σ, the flow depth h, and the channel-wall profiles $u_w(z)$ and $T_w(z)$ of downslope velocity and granular temperature. Since previous authors attempted to predict slightly different seismic properties and used slightly different flow properties, no directly applicable expressions are in the articles introducing the models (Kean et al., 2015; Lai et al., 2018; Farin et al., 2019; Bachelet, 2018). We therefore worked from equations (2) and (6); used the models' methods of estimating those equations' variables, as described in sections 1.2.1 and 1.2.2; and removed Green's functions as described in section 1.3, to predict the basal force's power spectrum rather than the power spectrum of a seismic station's response. Recalling that $g\cos\theta$ denotes base-normal gravitational acceleration, d the particles' mean diameter, and ρ their density, and approximating the flow area generating the measured signal by the instrumented plate's area $A = XY$ and the flow's mean volume fraction by $\phi = \sigma/\rho h$, these predictions could then be compared to the measured power spectra P_F.

The model introduced by Kean et al. (2015) predicts the seismic signal generated by a granular flow covering a certain area, using its surface velocity and the base-normal component of its weight per unit area. If the near-base velocity of the flow scales with its surface velocity, as Kean et al. (2015) suggests, then both will scale with the depth-averaged velocity $\bar{u}$, so to calculate predictions we estimated the velocity u of equation (2) with $\bar{u}$ and the impulse Δp with $\sigma g\cos\theta$, the measured base-normal component of the flow's weight per unit area. We may therefore write the model's prediction for P_F,

449 for signal periods $1/f$ well above the duration of a typical impact, as

$$\hat{P}_F^0 = K A \bar{u} (\sigma g \cos\theta)^2 / d^3. \tag{17}$$

451 K is a free parameter supposed equal to the product of a constant volume fraction; a
452 constant of proportionality between $\bar{u}$ and the near-base flow velocity; and a squared con-
453 stant of proportionality between the mean basal pressure and the typical impulse trans-
454 ferred by a basal impact. No indication is given as to its value, so it must be found by
455 fitting.

456 In contrast, the model introduced by Lai et al. (2018) requires no free parameter.
457 Noting that the experimental particles have a narrow diameter distribution, with 94th
458 percentile approximately equal to its mean d, and using the appropriate substitutions
459 for u and Δp in equation (2), the model's prediction for P_F is the constant

$$\hat{P}_F^0 = \pi^2 \rho^2 A d^3 \bar{u}^3 / 9, \tag{18}$$

461 with the implicit assumption that the volume fraction is equal to 1. Again, this predic-
462 tion is expected to be valid only for signal periods $1/f$ well above the duration of a typ-
463 ical impact.

464 The two models described by Farin et al. (2019) are developments of this model,
465 with that article's equation (16) developing the definition of the impulse denoted Δp in
466 our equation (2). Within the same frequency range as in prior paragraphs, the associ-
467 ated predictions for $P_F(f)$ are the constants

$$\hat{P}_F^0 = \pi^2 \rho^2 \phi A d^3 (1+e)^2 \xi(v) u_b^3 / 36, \tag{19}$$

469 where e is a constant coefficient of restitution; $\xi(v) \approx 0.053(1+5.6v^2)$ is a non-dimensional
470 function accounting for variation in impacts' geometry; and v and u_b define the veloc-
471 ities of base-impacting particles $u_b(\mathbf{e}_x + v\mathbf{e}_v)$, for randomly directed unit vector $\mathbf{e}_v$.

472 In the 'thin-flow' model, $u_b = \bar{u}$, whereas in the 'thick-flow' model $u_b = \chi\bar{u}d/h$
473 for velocity profile shape factor χ, assumed constant and between 1 and 1.5. The model-
474 specific parameters are e, v and χ, which all contribute to the prefactor and so cannot
475 be individually determined via fitting. We therefore take $e = 0.9$, consistent with the
476 rebound heights of particles dropped onto the instrumented plate; take $\chi = 1.25$, con-
477 sistent with the velocity profiles measured at the channel's wall; and fit the free param-

eter υ, corresponding to the normalised standard deviation of base-impacting particles' velocities. Farin et al. (2019)'s derivation of ξ makes unphysical assumptions (e.g. that impacting particles' velocities differ from $u_b \mathbf{e}_x$ by an exactly constant magnitude υu_b and that, for each impact velocity, all possible impact locations are equally likely), so the best-fit value of υ for an otherwise-accurate model will not exactly equal the true normalised standard deviation, but a model cannot be said to be accurate unless this best-fit value is a physically reasonable approximation. Specifically, the energy associated with velocity fluctuations is drawn from the mean flow and dissipated rapidly, so that we expect the typical magnitude of velocity fluctuations to be less than the mean velocity, and hence a condition for model accuracy is that $\upsilon < 1$.

To further assess the assumptions of the 'thick-flow' and 'thin-flow' models, we extended each model to higher frequencies. Farin et al. (2019) assumes binary, elastic, normal interactions during impacts, with impact velocities such that particle deformation in our experiments will be quasistatic and the Hertz theory described in S3 will apply. Applying this theory to the impact velocities and geometry assumed by Farin et al. (2019), we therefore compute predictions for P_F over a larger frequency range than that considered by the original article, as

$$\hat{P}_F(f) = \frac{\int_{S^2} \mathrm{d}^2\mathbf{e}_\upsilon \int_{S^2_{\pi/6}} \mathrm{d}^2\mathbf{e}_n \left(u_n \mathbf{e}_n \cdot \mathbf{e}_z\right)^2 \zeta(f\tau)\mathcal{H}\left(u_n\right)}{\int_{S^2} \mathrm{d}^2\mathbf{e}_\upsilon \int_{S^2_{\pi/6}} \mathrm{d}^2\mathbf{e}_n \left(u_n \mathbf{e}_n \cdot \mathbf{e}_z\right)^2 \mathcal{H}\left(u_n\right)} \hat{P}_F^0 \tag{20}$$

for unit sphere S^2; unit spherical cap $S^2_{\pi/6}$ with maximum polar angle $\pi/6$; normal impact velocity $u_n = u_b(\mathbf{e}_x + \upsilon\mathbf{e}_\upsilon) \cdot \mathbf{e}_n$; impact timescale $\tau(u_n)$ as defined by equation (3); non-dimensional function ζ as introduced in equation (4); and Heaviside step function $\mathcal{H}$.

Finally, the model described in Bachelet (2018) already predicts P_F over a large frequency range. Substituting equations (7) into (6) and moving from the well-defined particle layers considered in the thesis to the continuous profiles measured in our experiments, the predicted power spectral density of the basal force is

$$\hat{P}_F(f) = \frac{4\pi}{9}\phi A\rho^2 d^3 \int_0^h u'_w(z)T_w(z)\zeta\left(f\tau_w(z)\right)e^{-\gamma z}\,\mathrm{d}z, \tag{21}$$

where u'_w is the derivative of u_w; ζ is the non-dimensional function in equation (4); impact timescale $\tau_w(z)$ is defined with respect to $T_w(z)$ as τ_j is to T_j in equation (7); and constant γ is a free parameter, to be determined by fitting.

508   We compare these predictions to the measured power spectra P_F in section 3.3, but

509   first we define the time period and the frequency-space properties used for the compar-

510   ison, by considering the evolution of the flow (section 3.1) and the form of the power spec-

511   trum of the basal force (section 3.2).

3 Results

3.1 Evolution of the Flow

514   In each experiment, the flow passing a given point evolved through four distinct

515   stages: I) precursory saltation of particles released at the start of the experiment; II) ar-

516   rival of the dense flow's front; III) steady flow; and IV) decay of the flow. These corre-

517   sponded to different signals measured at the instrumented plate, as illustrated for two

518   different experiments in Figure 3.

519   As Figure 3 illustrates, saltating particles in stage I contributed little to the out-

520   flow mass M and to the net downslope and normal forces F_x and F_z, with an implied

521   number density of around one particle per cm^2 of plate surface, but such particles ap-

522   plied basal forces with significant spectral density P_F across a wide frequency range. Sim-

523   ilarly, the dense front's arrival in stage II had a short duration, but was associated with

524   an intense, broad power spectrum of basal force, as high-velocity, surficial particles reached

525   the front and impacted the plate. In general, as in Figure 3a, the power spectrum at high

526   frequencies then dropped during stages III and IV, indicating that impact velocities in

527   the dense flow's bulk were lower than those of high-velocity saltating particles. For 'transitional-

528   regime' flows, however, P_F remained the same during stages II and III, as in Figure 3b,

529   reflecting the continued saltation within each flow that defines this regime.

530   Such variation of signal properties between different experiments is summarised in

531   Table 1. With increasing channel incline $\tan\theta$ and release gate height h_g, the duration

532   of stage I decreased rapidly and that of stage II decreased slightly, as the speed of the

533   dense flow front increased to the speed of saltating particles. Since the same changes greatly

534   increased the high-frequency spectral density P_F of the plate-normal force during stage

535   III, which had duration determined by the reservoir's capacity and decreasing with h_g,

536   the contribution of stage I to the total generation of seismic energy decreased from around

537   70 % to less than 0.1 %, while the contribution of stage II remained between around 10 %

538   and 20 %, and the contributions of stages III and IV increased. In contrast to this pat-
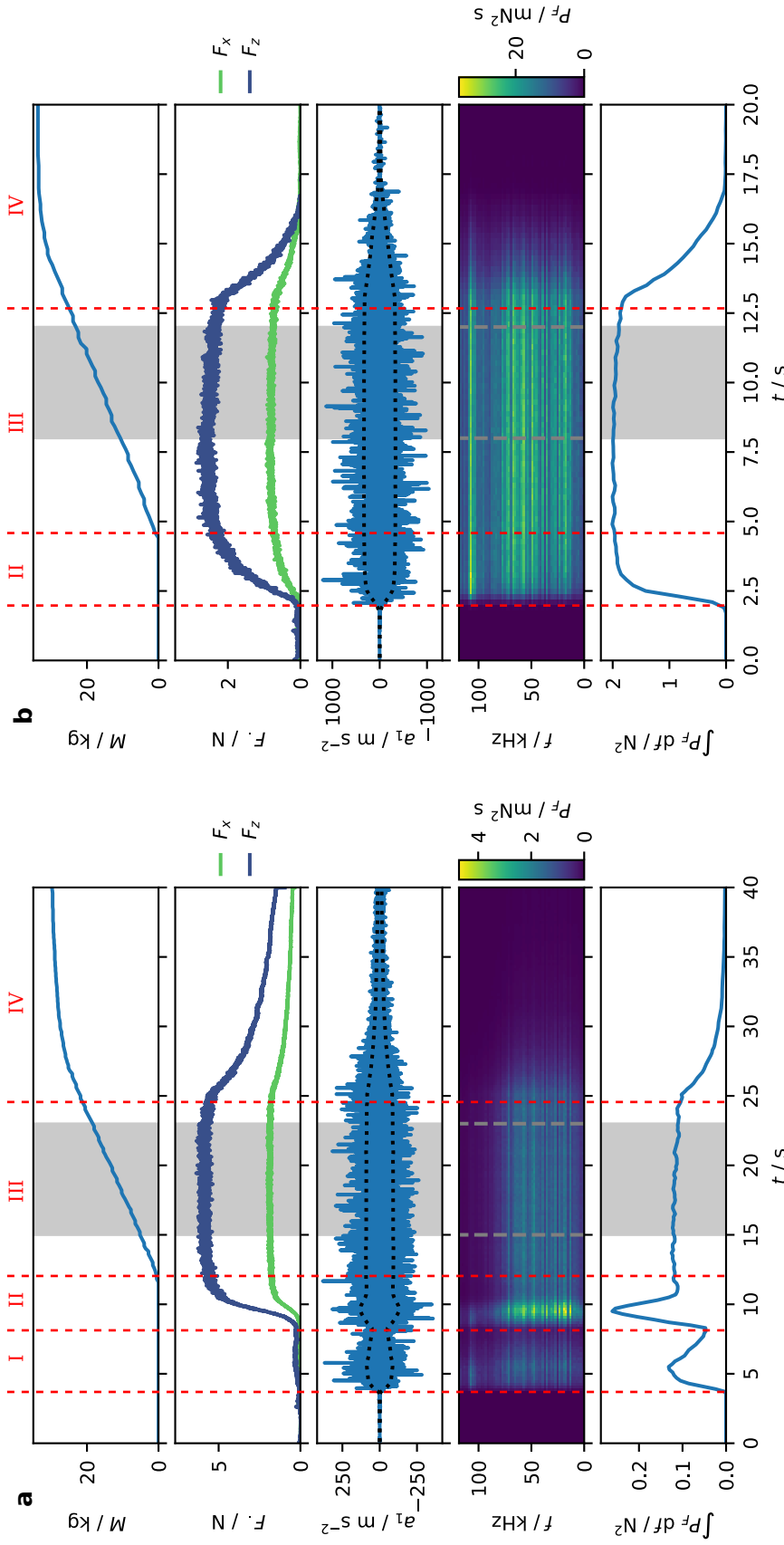
Figure 3. *Examples of flow properties' evolution over time.* Plots over time t of the cumulative outflow mass M; the net downslope and normal forces F_x and F_z applied to the instrumented plate; a measured normal plate acceleration a_1, with envelope indicated by dotted lines; the power spectral density P_F of the plate-normal basal force; and the integral of this power spectrum, which equation (25) shows to be proportional to the seismic power transmitted to the instrumented plate. a) A dense flow at a channel incline $\tan\theta = 0.44$ ($\theta = 23.7°$), with a release gate height $h_g = 20\,\mathrm{mm}$. b) A transitional-regime flow, with $\tan\theta = 0.52$ ($\theta = 27.5°$) and $h_g = 28\,\mathrm{mm}$. Flow stages I to IV are labelled, where present, and the shaded region indicates the period of steady flow recorded by the camera, $t_d < t < t_d + \Delta t_c$.

Table 1.   *Properties of the flow's stages of evolution. F_z and P_F are as defined in section 2.2, while f_c is the frequency at which P_F drops to half its mean value pre-maximum. Arrows ($\rightarrow$) indicate ranges over time in an experiment, while hyphens ($-$) represent the ranges over different experiments. $\bullet$ indicates the value for dense flows and $\circ$ for transitional-regime flows, wherever they differed significantly.*

Flow stage	I	II	III	IV
Durations / s	$0 - 40$	$2 - 8$	$4 - 150$	$5 - 20$
F_z / N	$O(0.1)$	$0 \rightarrow (1 - 10)$	$1 - 10$	$(1 - 10) \rightarrow O(1)$
f_c / kHz	> 100	> 90	$\bullet 70 - 110$ $\circ > 100$	$\bullet 70 - 110$ $\circ > 100$
$\int P_F \, \mathrm{d}f$ / N^2	$O(0.1)$	$0.02 - 2$	$0.003 - 3$	$(0.003 - 3) \rightarrow 0$

539   tern of variation, the net normal force F_z increased with h_g but, for each h_g, decreased

540   with $\tan\theta$, as the same flux of particles was maintained by a thinner flow, travelling faster.

541   These opposing trends indicate the independence of F_z and $P_F(f)$ for $f \neq 0$, with the

542   former the mean force applied by the flow, and the latter associated with the force's fluc-

543   tuations about this mean.

544   In this article, we restrict our attention to stage III of the flow's evolution, in which

545   the flow's steadiness ensured that all measurements were of the same flow state. Specif-

546   ically, between different $\Delta t = 0.2\,\mathrm{s}$ time intervals within the duration Δt_c of steady flow

547   recorded by the camera, the per-second rate of change of outflow mass M had a stan-

548   dard deviation of around 10 % of its mean value, while the standard deviations of F_x and

549   F_z were around 1 % and that for $\int P_F \, \mathrm{d}f$ around 5 %. Similarly, we examined the pro-

550   files of kinematic properties at the channel wall, averaged in turn over each decile of time

551    $t_d + n\Delta t_c/10 \; < \; t \; < \; t_d + (n + 1)\Delta t_c/10$ within the period recorded by the camera.

552   Within the flow, kinematic properties at the channel wall were steady over time, in the

553   sense that the values of $\phi_w(z)$, $\mathbf{u}_w(z)$ and $T_w(z)$ varied by at most a few percent over

554   time, for each z satisfying $\phi_w(z) > \max_z \phi_w(z)/2$.
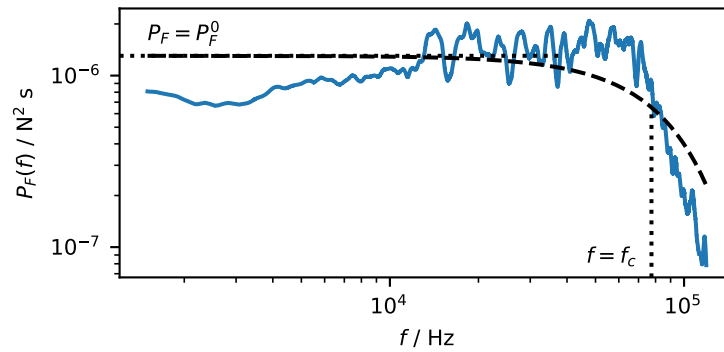
Figure 4. *Example of the plate-normal force's power spectral density during steady flow.* The power spectrum corresponds to the same experiment as Figure 3a, with channel incline $\tan\theta = 0.44$ ($\theta = 23.7°$) and release gate height $h_g = 20\,\text{mm}$. The dotted lines indicate the corner frequency $f_c = 77.5\,\text{kHz}$ and the low-frequency amplitude $P_F^0 = 1.29\,\text{mN}^2\,\text{s}$. The dashed line indicates the Hertzian power spectrum fit to these values, corresponding to 4000 Hertzian impacts per second of the experimental particles on the plate's surface, each at normal velocity $0.9\,\text{m}\,\text{s}^{-1}$.

3.2 Power Spectrum of the Basal Force

Averaging over this period of steady flow, by taking $\Delta t = \Delta t_c$ in equation (12), we calculated the power spectrum of the base-normal force applied by the flow to the plate and find it to be consistent with impacts of short duration. As in the example shown in Figure 4, the power spectral density $P_F(f)$ is approximately constant over a large frequency range and displays the same decay beyond a given corner frequency as Hertz theory predicts for a single impact. The fluctuations around this trend with varying frequency f are consistent between different experiments, as may be seen in Figure 3, and are systematic errors arising from variation in the density of the plate's resonant modes in frequency space, as discussed in S7.

We described the power spectrum by two quantities: its low-frequency amplitude P_F^0 and its corner frequency f_c. We calculated f_c as the frequency at which $P_F(f)$ drops to half its mean pre-maximum value, so that for a Hertzian impact it would be equal to approximately $0.208/\tau$, for the timescale τ defined in section 1.2.2 and S3. Any such comparison between f_c and a theoretical corner frequency is unlikely to be exact, due to systematic errors in our measured power spectra P_F, and this is reflected by the mismatch

–22–

Table 2. *Summary of model testing.* For each of the existing models described in section 1.2, we list those of the flow measurements defined in section 2.2 that are required to predict the flow's high-frequency seismic signal. We further record the equation for predictions $\hat{P}_F^0$; the free parameter value for which such predictions best fit measurements; and the geometric standard error $\epsilon = \exp\left[\sqrt{\frac{1}{N}\sum \ln(P_F^0/\hat{P}_F^0)^2}\right]$ of these predictions.

Model	Inputs	Equation	Best-fit parameter	ϵ
Kean et al. (2015)	$\bar{u}$, σ, θ	(17)	$K = 4.0 \times 10^{-16}\,\mathrm{m}^4\mathrm{s}^2$	4.2
Lai et al. (2018)	$\bar{u}$	(18)	n/a	18.5
Farin et al. (2019)	$\bar{u}$, σ, h	(19)		
'thick-flow'			$\upsilon = 9.8$	3.2
'thin-flow'			$\upsilon = 0.51$	2.1
Bachelet (2018)	σ, h, u_w, T_w	(21)	$\gamma = 0\,\mathrm{m}^{-1}$	3.9

between theoretical and experimental results in Figure 4. However, our measurements of f_c were sufficiently robust that we calculated P_F^0 as the mean value of P_F over all frequencies less than $f_c/2$. We could then compare these experimentally measured values with the model predictions, computed as described in section 2.3.

3.3 Tests of Existing Models for Flows' Seismic Signals

To assess the model predictions described in section 2.3, we compared their predictions $\hat{P}_F^0$ for the low-frequency value of the basal force's power spectrum to the measured values P_F^0. Where possible, we also inferred a prediction $\hat{f}_c$ for the corner frequency of the basal force's power spectrum, as the frequency at which $\hat{P}_F(f)$ dropped to half its maximum value, and we compared this prediction with the measured value f_c. Where a model had a free parameter, we used the parameter value that minimised the sum over all experiments of $\ln(P_F^0/\hat{P}_F^0)^2$, which was equivalent to minimising the typical logarithmic error or maximising the model likelihood under the assumption that measurements were log-normally distributed about their predicted values (see S9). Table 2 lists these best-fit parameter values and Figure 5 shows the results of the comparisons.
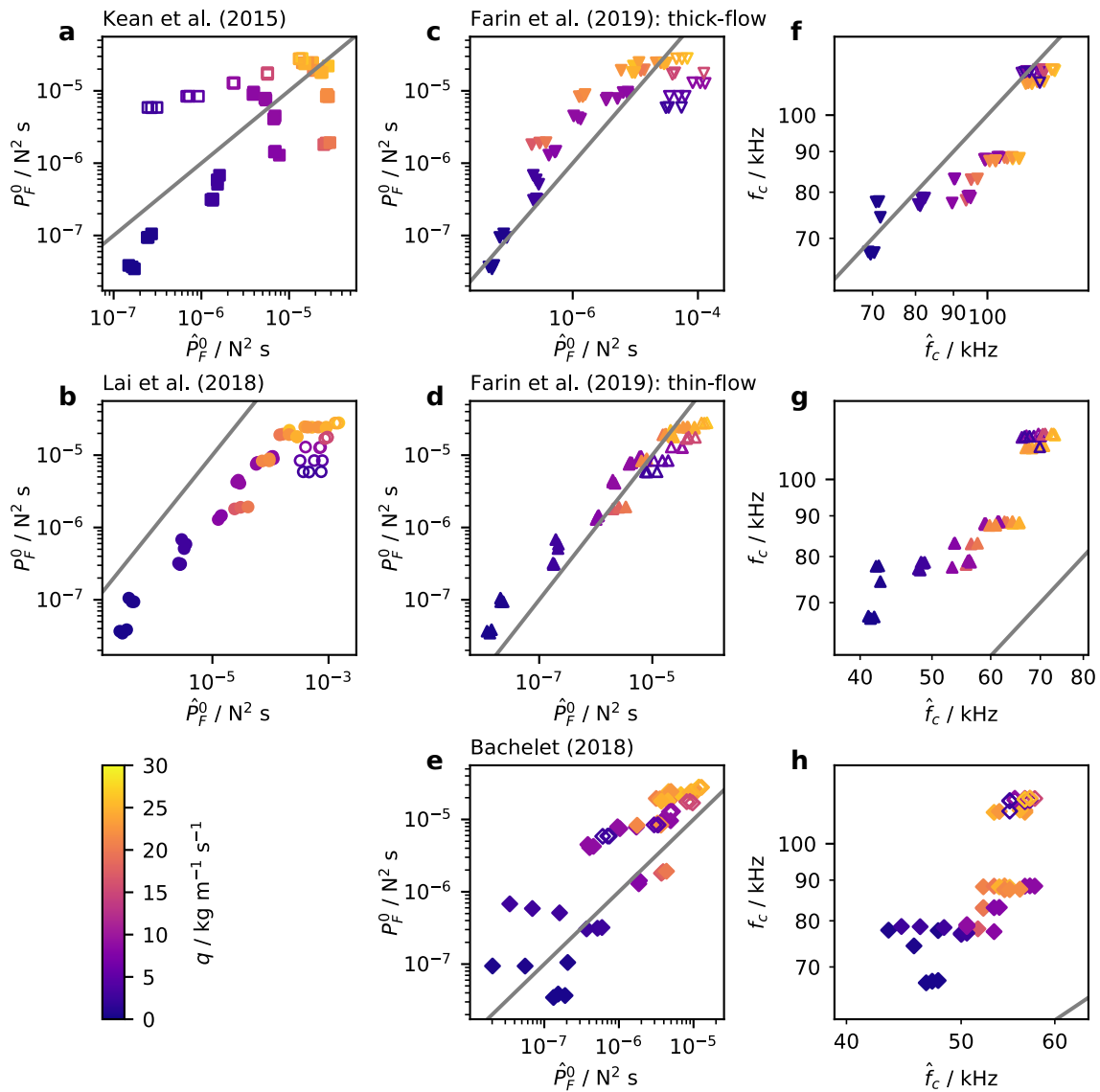
Figure 5. *Comparison between models' predictions (x-axes) and experimental measurements (y-axes) for the basal force's power spectrum.* Plots f, g, and h represent predictions for the corner frequency of the basal force's power spectrum, while all others represent predictions for the power spectral density's value at frequencies well below this corner frequency. In all plots, the grey line represents perfect agreement between predictions and measurements, colours indicate each experiment's mass flux q per unit channel width, and unfilled symbols represent experiments for which the flow was in the transitional regime.

586   The model introduced by Kean et al. (2015) predicts P_F^0 poorly, due largely to its

587   incorrect assumption of proportionality between the pressure fluctuations relevant to P_F^0

588   and the mean pressure $\sigma g \cos\theta$ used as input. To best fit the measurements, the free pa-

589   rameter K had to take a value of $4.0 \times 10^{-16}\,\mathrm{m^4 s^2}$, with a magnitude unforeseeable from

590   the model's assumptions, and even then predictions often differed from measurements

591   by an order of magnitude (Figure 5a). Notably, the model's predictions $\hat{P}_F^0$ decrease for

592   flows at higher channel inclinations or in the transitional regime, for which the mean pres-

593   sure is lower, whereas such flows' higher impact energies in fact resulted in higher pres-

594   sure fluctuations and so larger measured values P_F^0.

595   In contrast, the model introduced by Lai et al. (2018) accurately predicted vari-

596   ation in P_F^0 between experiments, with predictions for dense flows consistently 3 to 10

597   times larger than the measured values (Figure 5b). For transitional-regime flows, the pre-

598   dictions' errors are larger, due to the model's implicit assumption that the volume frac-

599   tion is equal to one.

600   Surprisingly, of the two models described by Farin et al. (2019), the model derived

601   for flows thicker than the largest particles is less accurate than that derived for thin flows,

602   with the former requiring an unphysical best-fit value for the ratio υ between the mag-

603   nitudes of velocity fluctuations and of the mean velocity. For the 'thick-flow' model, we

604   required $\upsilon = 9.8$ for predictions $\hat{P}_F^0$ to be as large as measurements P_F^0 and, in that case,

605   the predictions were too large for the transitional-regime flows (Figure 5c). For the 'thin-

606   flow' model, meanwhile, the best-fit value was $\upsilon = 0.51$, which is physically reasonable

607   and provides an excellent fit of $\hat{P}_F^0$ to P_F^0 over all experiments (Figure 5d).

608   This difference between the 'thick-flow' and 'thin-flow' models' best-fit values of

609   υ is reflected in the predictions $\hat{f}_c$ they implied for the corner frequency of the basal force's

610   power spectrum, calculated according to our extensions of these models using equation

611   (20). The higher υ required for the 'thick-flow' model results in higher predictions $\hat{f}_c$,

612   matching the measured values f_c (Figure 5f), whereas for the 'thin-flow' model predic-

613   tions are consistently approximately 30 % smaller than the measured values (Figure 5g).

614   Predicted corner frequencies $\hat{f}_c$ are as large as measurements f_c only for typical impact

615   velocities six times larger than the flows' mean velocities, suggesting that our measure-

616   ments f_c were slight, but systematic, overestimates.

Finally, the predictions of the model described in Bachelet (2018) followed the correct trend but had a wide dispersion (Figure 5e). The free parameter γ, representing signal attenuation within the flow, had best-fit value 0, indicating that the unattenuated contributions of all synthetic impacts are necessary for $\hat{P}_F^0$ to be large enough to compare to P_F^0. Even then, the lower energies of synthetic impacts are reflected in predictions $\hat{f}_c$ for the power spectrum's corner frequency that are even lower than those of our extension to Farin et al. (2019)'s 'thin-flow' model (see Figure 5h).

Overall, of the five models, the 'thin-flow' model described in Farin et al. (2019) best fits the results from our experiments. While the fit is imperfect, the predictions $\hat{P}_F^0$ of this model differ from the measured values P_F^0 by a typical factor of 2.1, lower than that for the other models, and the model's accuracy is approximately equal across the entire range of experiments, including for the flows in the transitional regime. Constructing a statistical model for each physical model, by assuming $\ln P_F^0$ was normally distributed about $\ln \hat{P}_F^0$ with constant variance, the 'thin-flow' model is also the preferred model by the Akaike information criterion (see S9), indicating that its additional free parameter compared to the Lai et al. (2018) model is worthwhile in an information theoretic sense. This analysis did not compare models' predictions to the measured corner frequencies f_c, due to the likelihood of systematic error in the latter, but our extensions to the models of Farin et al. (2019) both predicted a trend in $\hat{f}_c$ consistent with measurements.

4 Discussion

4.1 Velocity Profiles and the 'Thin-flow' Model

That the 'thin-flow' model best predicts the experimental results is surprising, because we do not expect the velocity profile within the flow to be consistent with the model's assumptions. The 'thin-flow' model assumes that particles at the flow's base move across the instrumented plate's surface at approximately the flow's mean velocity, whereas previous authors suggest that the plate's roughened surface should impose a no-slip condition on the flow, in the sense that particles' velocities should tend to zero towards the flow's base (GDR MiDi, 2004; Jing et al., 2016). Furthermore, as the example of Figure 6 demonstrates, the velocity profiles we observe at the channel's wall are consistent with this no-slip condition (which we note is distinct from any micromechanical condition on rolling or sliding at particle contacts).
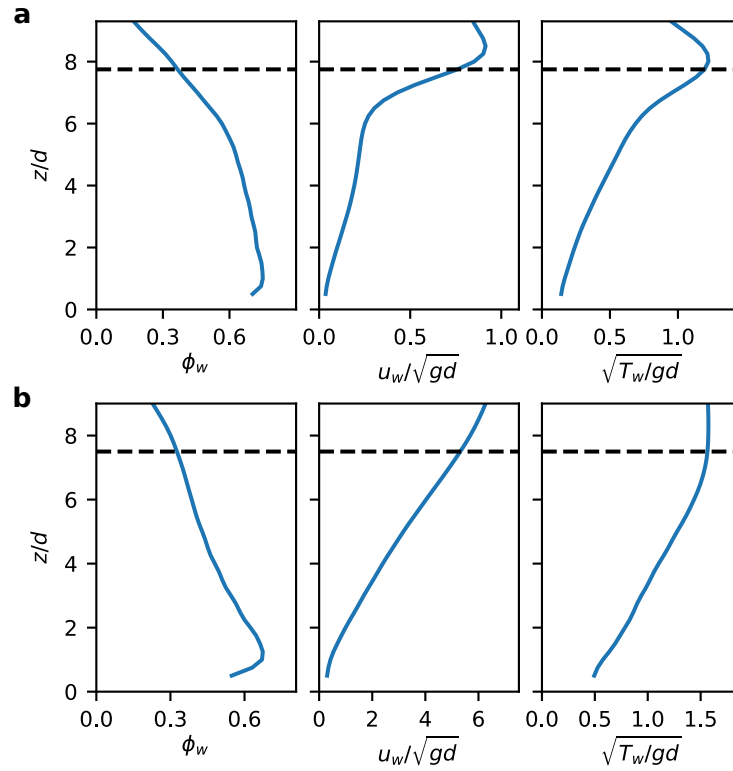
Figure 6. *Examples of kinematic properties' steady profiles at the channel wall.* Profiles are estimates from particle tracking velocimetry of the relative volume fraction ϕ_w, the downslope velocity u_w, and the square root $\sqrt{T_w}$ of the granular temperature, non-dimensionalised by $\sqrt{gd} = 0.14$, while the dashed lines represent the flow thicknesses h inferred from the profile of ϕ_w. Profiles are taken from the same experiments as for Figure 3: a) a dense flow at channel incline $\tan\theta = 0.44$ ($\theta = 23.7°$) with release gate height $h_g = 20$ mm; and b) a transitional-regime flow at channel incline $\tan\theta = 0.52$ ($\theta = 27.5°$) with release gate height $h_g = 28$ mm.

We propose two possible explanations for the success of the 'thin-flow' model. The first is that the instrumented plate's flow-induced vibration reduces the effective friction between it and the flow, leading to basal slip and a basal flow velocity closer to the flow's mean velocity. The second is that basal particles have low velocities, but that impacts away from the flow's base make significant contributions to the basal force exerted by the flow, in such a way that the total contribution of these impacts scales with the mean velocity of the flow.

The first explanation is supported by the literature on frictional weakening and by measurements of the plate's effective friction coefficient with the flow. The reduction by vibration of a granular medium's effective friction has been documented in discrete element simulations (e.g. Capozza et al., 2009; Ferdowsi et al., 2014; Lemrich et al., 2017) and experiments (e.g. Johnson et al., 2008; Dijksman et al., 2011; Lastakowski et al., 2015), with suggestions for the necessary vibration amplitude being a particle strain of order 10^{-6} (Ferdowsi et al., 2014), a velocity of order $100\,\mu\mathrm{m\,s}^{-1}$ (Lastakowski et al., 2015), and an acceleration of order $0.1g$ (Dijksman et al., 2011). Even in the experiments in which the plate vibration amplitudes during steady flow were lowest, the plate had approximate root mean square normal displacement $10\,\mathrm{nm}$, velocity $100\,\mu\mathrm{m\,s}^{-1}$, and acceleration $20\,\mathrm{m\,s}^{-2}$, so a vibration-induced reduction in friction appears viable. Furthermore, the effective friction coefficients μ that we measure between the plate and the flow are too low to prevent basal slip on the surface of the plate, with Figure 7a showing that $\mu < \tan\theta$ for all channel inclines $\tan\theta$. This implies that basal particles accelerate across the plate's surface, towards the flow's mean velocity.

On the other hand, we do not directly measure any increases in velocity associated with basal slip. Over the $8\,\mathrm{cm}$ distance downslope captured by the high-speed camera, averaging over each flow's depth and each $4\,\mathrm{cm}$ half-window, the mean downslope velocities measured at the sidewall are uniform to within $10\,\%$. Away from the sidewalls, Tsang et al. (2019) suggests that a granular flow will adjust to a change in basal boundary conditions over a lengthscale of order $\bar{u}^2/g$, for mean flow velocity $\bar{u}$ and gravitational acceleration g. This lengthscale varies in our experiments from $0.5\,\mathrm{mm}$ to $0.1\,\mathrm{m}$, so that we would expect the effects of any basal slip to become evident at the flow's surface within the length of the instrumented plate. However, having conducted particle image velocimetry with images captured by an overhead camera, for a flow at a channel incline $\tan\theta = 0.46$ ($\theta = 24.7°$) and with release gate height $h_g = 20\,\mathrm{mm}$, we were unable to distin-
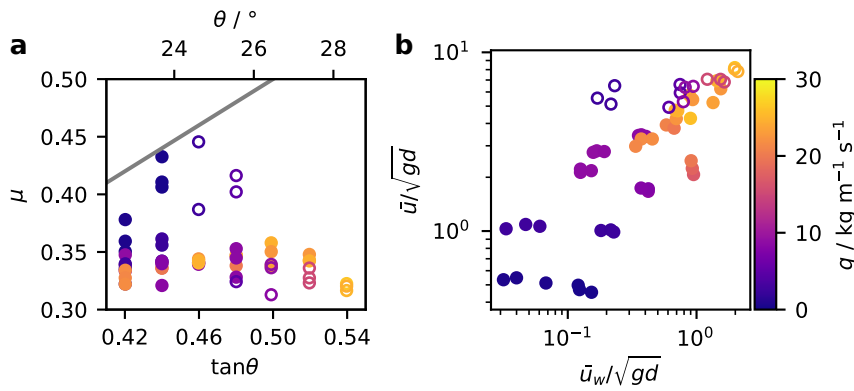
Figure 7. *Discrepancies between model assumptions and measurements.* a) Measurements of the effective friction coefficient μ between the instrumented plate and the flow fall consistently below the condition $\mu = \tan\theta$ for zero basal slip (grey line). b) The depth-averaged particle velocity measured at the channel wall $\bar{u}_w$ is poorly correlated with the mean velocity $\bar{u}$ calculated from bulk flow properties. Colours indicate each experiment's mass flux q per unit channel width, and unfilled symbols represent experiments for which the flow was in the transitional regime.

681 guish whether the flow's surface's slight acceleration across the plate was induced by the

682 plate, or was simply a continuation of the flow's acceleration towards a uniform state.

683 Similarly, we attempted to detect changes in the velocity of basal particles, via Jop et

684 al. (2005)'s method of examining soot erosion from an inserted metal plate, but our at-

685 tempts were frustrated by the energetic particles' rapid erosion of soot during the inser-

686 tion and removal of the plate.

687 Consequently, the second explanation remains feasible, with good reasons why the

688 model of Bachelet (2018), despite being derived to describe the contributions of impacts

689 throughout the flow's depth, might describe them less well than the 'thin-flow' model.

690 Firstly, the Bachelet (2018) model uses profiles u_w and T_w that are measured at the chan-

691 nel's wall and may not be representative of those in the flow's interior. In fact, the mean

692 particle velocity measured at the channel wall $\bar{u}_w$ correlates poorly with the mean ve-

693 locity $\bar{u}$ inferred from bulk measurements (see Figure 7), while the monotonically increas-

694 ing profiles $T_w(z)$ differ from the S-shaped profiles that previous authors propose for gran-

695 ular temperature profiles in the flow's interior (Hanes & Walton, 2000; Silbert et al., 2001;

696 Gollin et al., 2017). Secondly, Bachelet (2018) may suggest an incorrect dependence of

697 the seismic signal on these profiles, with a particularly strong assumption being that of

698   a frequency-independent attenuation constant γ. We were unable to dramatically im-

699   prove the predictions of Bachelet (2018)'s model by modifying its inputs, e.g. by mul-

700   tiplying the profiles $u_w(z)$ and $\sqrt{T_w(z)}$ by $\bar{u}/\bar{u}_w$, but, under a different model for the

701   contributions of impacts throughout the flow, such contributions could explain the re-

702   lationship observed between the mean velocity $\bar{u}$ and the basal force's power spectrum

703   P_F.

704   To test which explanation accounts for the success of the 'thin-flow' model, we sug-

705   gest that our experimental conditions be replicated with discrete element simulations.

706   In such simulations, a suitably roughened base could be fixed in position to prevent any

707   vibration-induced reduction of its effective friction coefficient and any basal slip, as records

708   of base-adjacent particles' velocities could verify. If the 'thin-flow' model continued to

709   be accurate, then the first, 'basal slip' explanation would be disproven. Records of par-

710   ticle velocities throughout the flow would then permit variants of Bachelet (2018)'s model

711   to be tested and their assumptions examined, using base-normal profiles of velocity and

712   granular temperature measured within the flow's bulk rather than at its edge, to explain

713   the 'thin-flow' model's accuracy. If the 'thin-flow' model were no longer accurate, how-

714   ever, then our first explanation would be proven and the model shown to apply only to

715   flows with basal slip. The recorded particle velocities would then permit development

716   of a different model, by which a small number of flow parameters could predict the seis-

717   mic signal generated by flows without basal slip, analogous to the use of $\bar{u}$ in the 'thin-

718   flow' model, or of the inertial number to predict a dense granular flow's kinematic prop-

719   erties.

720   **4.2 The Inertial Number and the Seismic Signal**

721   Within a granular flow, the inertial number I is a local, non-dimensional mean shear

722   rate, which previous authors suggest will uniquely determine all other local, non-dimensional

723   flow parameters (GDR MiDi, 2004; da Cruz et al., 2005; Jop et al., 2006). This '$\mu(I)$'

724   framework will not apply where a) the flow's rheology is 'non-local', in the sense that

725   the internal stress depends on derivatives of the strain rate rather than on only the strain

726   rate's local value (Clark & Dijksman, 2020), or b) particles are sufficiently agitated that

727   kinetic theory describes their motion better than a mean shear rate (Goldhirsch, 2003).

728   If, however, the '$\mu(I)$' framework applies within a two-dimensional, steady, uniform shear

729   flow above a plate with incline $\tan\theta$, a macroscopic force balance implies that I is con-

730   stant and can be estimated from bulk measurements of the flow's mean velocity $\bar{u}$, vol-

731   ume fraction ϕ, and depth h (Jop et al., 2005), as

$$\hat{I} = \frac{5\bar{u}d}{2h\sqrt{\phi gh\cos\theta}}. \tag{22}$$

733   Even if our experimental flows were uniform, without basal slip, the local inertial num-

734   bers within them will have differed significantly from $\hat{I}$, with non-locality being partic-

735   ularly significant within slow, thin flows; particles being particularly agitated within transitional-

736   regime flows; and friction at the channel's walls altering the force balance. We neverthe-

737   less calculated $\hat{I}$ as a descriptor for each flow, with $\phi = \sigma/\rho h$ for flow mass per unit area

738   σ and particle density ρ and with other quantities defined in sections 2.1 and 2.2. We

739   see in Figure 8a that the '$\mu(I)$' framework applies for the dense experimental flows, in-

740   sofar as the local, non-dimensional parameter $\tan\theta$ is closely related to $\hat{I}$.

741   To examine the relevance to each flow's seismic signal of this inertial number es-

742   timate $\hat{I}$, we define a non-dimensional parameter $\delta\mathcal{F}^2$ expressing the mean squared mag-

743   nitude of high-frequency basal force fluctuations on the instrumented plate, normalised

744   by the mean basal force. From the low-frequency amplitude P_F^0 and corner frequency

745   f_c of the basal force's power spectrum, and from gravitational acceleration g, inclina-

746   tion angle θ, plate length X and width Y, and measured mass overburden σ, we calcu-

747   late for each flow

$$\delta\mathcal{F}^2 = \frac{2P_F^0 f_c}{(XYg\sigma\cos\theta)^2}. \tag{23}$$

749   To understand this definition, we recall from equation (8) that $XYg\sigma\cos\theta$ is the mean

750   normal force applied by the flow to the instrumented plate, over the time interval Δt_c

751   of steady flow recorded by the camera. Meanwhile, as Figure 4 indicates, $2P_F^0 f_c$ approx-

752   imates the integral of the symmetric power spectral density $P_F(f)$ over all f with $|f| >$

753   1 kHz, this being the lowest frequency accessible to our measurements. Recalling that

754    $\tilde{F}(f)$ is the Fourier transform over Δt_c of the normal force applied to the plate, $P_F(f) =$

755    $|\tilde{F}(f)|^2/\Delta t_c$. Combining these links and then applying the Plancherel theorem (Plancherel

756   & Mittag-Leffler, 1910) to move to the time domain,

$$2P_F^0 f_c \approx \frac{1}{\Delta t_c}\int_{|f|>1\,\mathrm{kHz}}|\tilde{F}(f)|^2\;\mathrm{d}f = \frac{1}{\Delta t_c}\int_{\Delta t_c}|\delta F(t)|^2\;\mathrm{d}t, \tag{24}$$

758   where δF is the fluctuating normal force on the plate, high-pass-filtered above 1 kHz. As-

759   suming that pressure fluctuations are spatially uncorrelated on the lengthscale of the plate,

760   as discussed in S2, $2P_F^0 f_c$ will be proportional to the plate's area XY and $\delta\mathcal{F}^2$ to $1/XY$,
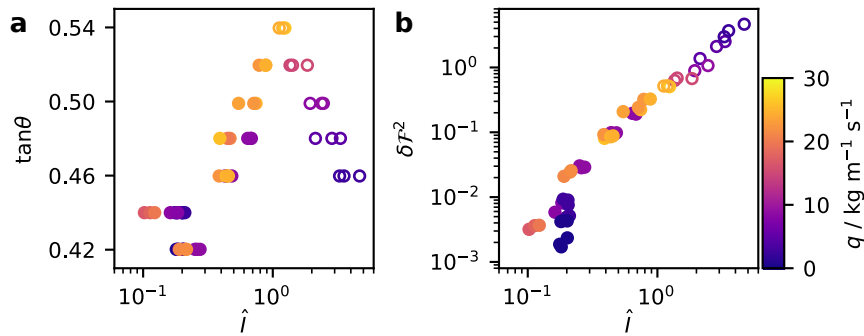
Figure 8. *Relations between the inertial number $\hat{I}$ estimated from bulk flow parameters and a) the channel incline $\tan\theta$, b) the normalised mean squared fluctuating force on the plate $\delta\mathcal{F}^2$. Colours indicate each experiment's mass flux q per unit channel width, and unfilled symbols represent experiments for which the flow was in the transitional regime.*

but $\delta\mathcal{F}^2$ can be thought of as a rescaling by d^2/XY of a local flow parameter, for mean particle diameter d.

Plotting $\delta\mathcal{F}^2$ against $\hat{I}$ for each flow, in Figure 8b, we see that this measure of the high-frequency seismic signal is well determined by the estimated inertial number. This relationship between non-dimensional, local flow parameters is in accord with the '$\mu(I)$' framework, with more energetic flows producing more energetic seismic signals, even for flows to which the '$\mu(I)$' framework is otherwise inapplicable.

However, it is unclear how it relates to the experimental results of Taylor and Brodsky (2017), in which the mean squared seismic accelerations generated by a torsional shear flow were directly proportional to estimates of the flow's inertial number. Whilst our results do not appear consistent with such direct proportionality, with δF^2 increasing much faster than $\hat{I}$, it is impossible to make a direct comparison without knowing the magnitude of the Green's function relating the accelerations discussed by Taylor and Brodsky (2017) to the forces imposed by that article's shear flow. Such Green's functions are essential in considering the seismic signal generated by a flow, and so in considering the application of our results to geophysical flows.

4.3 The Application of Our Results to Geophysical Flows

Our results concern the fluctuating forces exerted by laboratory granular flows upon the base on which they travel, so their application to landquake signals necessitates consideration of two things: the Green's function that determines a flow's seismic signal from the forces it exerts, and the differences between geophysical flows' forces and those that we've studied. We limit ourselves to describing the importance of an accurate Green's function, rather than defining one, and to discussing the adjustments involved in moving from laboratory to geophysical flows, rather than validating them, but we nevertheless propose tentative links between our results and the empirical relationships observed by previous authors.

4.3.1 The Importance of an Accurate Green's Function

The forces exerted by a geophysical flow determine a measurable seismic signal only via a Green's function, so an accurate Green's function is necessary to interpret any landquake signal. Here, we use our experimental seismic signals to show that this is true even of certain seismic properties that previous authors have used to describe geophysical flows, including both the rate of seismic energy emission and the relative amplitudes of different landquake signals with the same source and receiver locations.

For our experiments, the Green's function appears via equation (12), which relates the basal forces exerted by the flow to the accelerations they caused and indicates that, on a larger, denser, stiffer, or more lossy plate, the same force would result in smaller accelerations and hence a smaller seismic signal. Similarly, working from the derivation of this equation in S7, the total high-frequency seismic power transferred by the flow to the plate is given in terms of the basal force's power spectral density P_F by

$$\Pi_s \approx \frac{1}{4\sqrt{\rho_p H D}} \int_{1\,\mathrm{kHz}}^{\infty} P_F(f)\,\mathrm{d}f, \qquad (25)$$

dependent on plate density ρ_p, thickness H, and bending moment D. The proportion of flow energy dissipated by seismic emission is therefore a function of basal properties rather than of flow properties alone, which especially complicates comparisons between experimental and geophysical flows, such as Bachelet (2018)'s.

Furthermore, the Green's functions for seismic signals will depend differently on frequency f, so that basal properties will affect even the relative signal amplitudes of dif-

807 ferent flows with the same Green's function. For illustration, we consider the vertical ve-

808 locity response of a surficial receiver to a vertical, surficial point force, on an isotropic,

809 homogeneous, perfectly elastic half-space with Poisson ratio 0.25, material density ρ_g and

810 shear wave velocity c_s. For large source-receiver separation r, at leading order, Miller

811 and Pursey (1954) showed the power spectral density P_{v_r} of this response to be related

812 to the power spectral density P_F of the vertical basal force by

$$P_{v_r}(f) = \frac{1.20 f^3}{\rho_g^2 c_s^5 r} P_F(f), \tag{26}$$

814 which we compare to the mean velocity power spectral density over the accelerometers

815 in our experiments,

$$\bar{P}_{v_j}(f) = \frac{1}{4\Delta t} \sum_{j=1}^{4} \left(\frac{|\tilde{a}_j(f)|}{2\pi f} \right)^2 \approx \frac{\mathcal{P}Q}{16\pi(\rho_p H)^{3/2} XY\sqrt{D} f} P_F(f). \tag{27}$$

817 The mean squared velocity at the receiver, being the integral of $P_{v_r}(f)$ over all f, will

818 clearly be more sensitive to the corner frequency f_c of P_F than were the mean squared

819 velocities observed in our experiments. Figure 9 shows the consequence: approximating

820 mean squared velocities by integrating (26) and (27) between $1\,\mathrm{kHz}$ and f_c, there is no

821 constant conversion factor between the mean square velocities observed in our experi-

822 ments and those that would be observed if the same flows applied the same forces in an

823 idealised geophysical context. Even among signals with the same source and receiver lo-

824 cations, the Green's function determines the ratios between different signals' amplitudes,

825 so that a signal must be properly deconvolved to infer the properties of a flow's forces.

4.3.2 *Adjustments to Forces for Geophysical Flows*

827 Returning to consideration of such forces, the application of our results to geophys-

828 ical flows involves significant adjustments, firstly to the sizes of the flow and its constituent

829 particles and secondly to the flow's evolution.

830 Clearly, geophysical flows of interest will be more extensive than our experimen-

831 tal flows and will involve larger particles, but these changes will not alter the underly-

832 ing physics and simply necessitate adjustment of the values of flow area A and particle

833 diameter d in the models of section 2.3. According to these models, a flow identical to

834 those in our experiments, except with particles of radius $1\,\mathrm{m}$, should produce a seismic

835 force signal with power spectral density per unit flow area $\hat{P}_F(f)/A$, of order $(10^2$ to $10^6)\,\mathrm{N^2\,m^{-2}\,s}$

836 below a corner frequency f_c of order $100\,\mathrm{Hz}$. A more difficult adjustment is required to
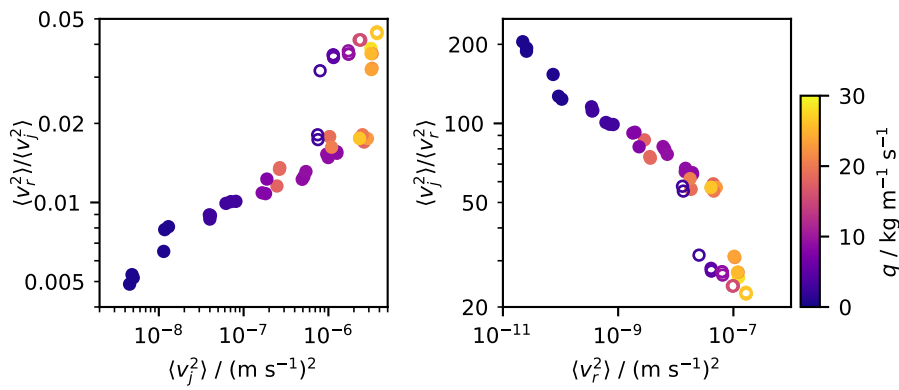
Figure 9. *Comparison between the mean squared seismic velocities $\langle v_j^2 \rangle$ observed in our experiments and the mean squared velocities $\langle v_r^2 \rangle$ that would be observed in an idealised geophysical context.* For the latter, we took $\rho_g = 2500 \, \mathrm{kg \, m^{-3}}$, $c_s = 1 \, \mathrm{km \, s^{-1}}$, and $r = 1 \, \mathrm{m}$ in equation (26), but other values would change only the prefactor. Colours indicate each experiment's mass flux q per unit channel width, and unfilled symbols represent experiments for which the flow was in the transitional regime.

account for the wide particle polydispersity typical of geophysical flows (Takahashi, 1981; Nishiguchi et al., 2012), which makes d hard to define and necessitates consideration of the segregation of particles by size that is well-documented within granular flows (e.g. Garve, 1925; Gray, 2018). Farin et al. (2019) proposes a promising approach for each given model, of dividing the flow into a coarse-grained front and a fine-grained tail and calculating for each a percentile of the particle size distribution that will be representative, but this proposal requires validation.

Other necessary changes relate to the flow evolution, stemming from differences in particles' coefficient of restitution and in the mechanism of their release. The glass beads in our experiments underwent collisions more elastic than are typical in geophysical flows (Kim et al., 2015), resulting in our observations of sustained saltation at relatively low channel inclinations. This implies that the precursory saltation of flow stage I, discussed in section 3.1, is unlikely to be significant for most geophysical flows, though it may be analogous to rock falls at high slope inclinations. Similarly, the energetic, saltating particles observed in the steady stage III of transitional-regime flows are likely to be rare in geophysical flows, though the coexistence of a dense core and a saltating layer is documented in snow avalanches (Pudasaini & Hutter, 2006). In fact, the entirety of the ex-

854   perimental flows' stage III is atypical of geophysical flows, since particles were released

855   from the experimental reservoir over a long period at a constant flux, whilst the release

856   of geophysical flows is rarely so steady or protracted. Therefore, our results should only

857   apply to individual stages of a geophysical flow, over which flow properties vary little enough

858   that the mean quantities we discuss are representative. Determination of quantities that

859   are representative of an entire flow requires further work.

4.3.3   Comparisons with Empirical Results

861   Nevertheless, we can tentatively link our measurements of experimental flows' forces

862   to the landquake signals of geophysical flows, by assuming the validity both of certain

863   adjustments to those forces and of certain restrictions to the Green's function linking geo-

864   physical forces to landquake signals. Firstly, we assume that any precursory saltation

865   of a geophysical flow contributes so insignificantly to the signal as to be negligible. Sec-

866   ondly, we suppose that the release mechanism and size distribution of geophysical par-

867   ticles significantly affect the signal only by determining the flow's duration and a rep-

868   resentative diameter of its particles. Thirdly, we assume that the signal's Green's func-

869   tion is constant over time and corresponds to transmission along a single wave path, with-

870   out significant dispersion in time. Finally, we consider the signals only at frequencies lower

871   than any force's power spectrum's corner frequency f_c, but high enough for the stochas-

872   tic impact framework and hence our results to apply.

873   Under these assumptions, the landquake signal v_r between times t_r and $t_r + \Delta t$

874   will only depend significantly on the forces exerted by the landslide between times t_s and

875     $t_s + \Delta t$, for some source-receiver delay $t_r - t_s$. Neglecting non-normal components, these

876   forces will have a power spectral density within the relevant frequency band that is equiv-

877   alent to those that we have studied and is well-described by the constant prediction $\hat{P}_F^0$

878   of Farin et al. (2019)'s 'thin-flow' model, for flow properties averaged between t_s and $t_s +$

879   Δt. Writing $\tilde{G}(f)$ for the relevant frequency-space Green's function and f_0 and f_1 for

880   the minimum and maximum frequencies under consideration, the mean squared ampli-

881   tude of the signal will be

$$\langle v_r^2 \rangle_{\Delta t} = \frac{2}{\Delta t} \int_{f_0}^{f_1} |\tilde{v}_r(f)|^2 \, \mathrm{d}f \approx 2\hat{P}_F^0 \int_{f_0}^{f_1} |\tilde{G}(f)|^2 \, \mathrm{d}f. \qquad (28)$$

883   Given this link, we can compare our results to the empirical relations discussed in

884   section 1.1. Qualitatively, the landquake signal's envelope will have the same shape as

885   the envelope of the time-retarded geophysical force, as Figure 3 shows to be the case for

886   our experimental forces and acceleration signals. Adjusting these envelopes by exclud-

887   ing the precursory saltation and shortening the artificially prolonged stage of steady flow,

888   our results therefore predict the distinctive 'spindle-shaped' signal envelopes associated

889   with geophysical granular flows (Suriñach et al., 2005). Quantitatively, our results sug-

890   gest that a flow's duration will equal its signal's, as in the empirical observations of e.g.

891   Deparis et al. (2008), though our experiments are unlike those of Farin et al. (2018) in

892   that our release mechanism prevents comparison with the observed empirical relation-

893   ship between potential energy loss and signal duration. Similarly, we cannot compare

894   our results to the observations of e.g. Norris (1994), that the flow volume is correlated

895   with the signal amplitude.

However, we can compare our results with other empirical relationships for the sig-
nal amplitude. Substituting equation (19) for $\hat{P}_F^0$ into equation (28) and assuming both
constant particle properties and a constant Green's function, our results suggest that a
flow of area A in which the particle volume fraction is ϕ and the mean flow velocity is
$\bar{u}$ will generate a signal with mean squared amplitude proportional to $\phi A \bar{u}^3$. Rearrang-
ing equation (22) for flow depth h and noting that the mean flow momentum per unit
area $q = \rho\phi h\bar{u}$, for particle density ρ, we recover that

$$q^3 = \frac{25\rho^3\phi^2 d^2\bar{u}^5}{4\hat{I}^2 g \cos\theta} \text{ and } \bar{u}^3 = \left(\frac{4\hat{I}^2 g q^3 \cos\theta}{25\rho^3\phi^2 d^2}\right)^{3/5}, \quad (29)$$

896   for bulk inertial number $\hat{I}$, representative particle diameter d, gravitational acceleration

897   g, and slope angle θ. Among flows with constant $\hat{I}$ and ϕ, the resulting landquake sig-

898   nals will therefore have root mean squared amplitude proportional to $A^{1/2}q^{9/10}\cos^{3/10}\theta$.

899   Whilst the assumption of constant $\hat{I}$ is very strong, this quantity is close to those found

900   empirically to be approximately proportional to landquake signal amplitude: the work

901   rate against friction used by e.g. Schneider et al. (2010), which will be equal to $\mu A q \cos\theta$

902   for basal friction coefficient μ, and the total flow momentum used by e.g. Hibert et al.

903   (2015), equal to Aq. Holding all else constant, the scalings $A^{1/2}$ and A correspond to spa-

904   tially separated impacts' signals being perfectly uncorrelated and perfectly correlated,

905   respectively, so S2 suggests that $A^{1/2}$ is likely to be a better approximation, while the

906   scalings $q^{9/10}$ and q are unlikely to be distinguishable in the field.

5 Conclusion

In conclusion, our experimental apparatus and data analysis permitted us to study the normal force exerted by a granular flow upon the base over which it travels, by measuring its high-frequency power spectral density and testing a range of existing models that predict this spectral density from the flow's properties. Figure 5 shows the 'thin-flow' model of Farin et al. (2019) to best predict the spectral density at frequencies well below its corner frequency and demonstrates that our extension of that model to higher frequencies, using Hertz theory, correctly predicts the corner frequency's behaviour. We've proposed that the success of the 'thin-flow' model, despite our experimental flows' thickness compared to their consituent particles, can be explained either by slip at each flow's base or by the contributions to the seismic signal of impacts throughout each flow's depth, and we've discussed the adjustments required to apply our results to the landquake signals generated by the forces of geophysical granular flows. Making such adjustments, under certain restrictive assumptions, the 'thin-flow' model's predictions are consistent with the empirical observation that a landquake signal's amplitude is approximately proportional to the momentum per unit area of the flow region that generated it.

Finally, our results are also relevant to two open questions on geophysical granular flows' dynamics: 1) the relation between the mean and fluctuating forces exerted by a flow; and 2) the low values of effective friction inferred for many geophysical flows. On the first question, previous authors have suggested that the typical magnitude of fluctuations is proportional to the magnitude of the mean force (McCoy et al., 2013; Hsu et al., 2014), but we show in Figure 8b that the ratio between the two, $\delta\mathcal{F}$, varies over two orders of magnitude between our experimental flows, dependent on a bulk inertial number. On the second, acoustic fluidisation is one of many possible explanations suggested for the low effective friction necessary to explain many geophysical flows' long runouts (Davies, 1982; Lucas et al., 2014), but we are not aware of it having been previously demonstrated without the application of external forcing. As Figure 7a illustrates, our measurements of μ show the effective friction taking values on the plate lower than the channel incline $\tan\theta$, which is implied to be its approximate off-plate value by both the downslope uniformity of the flow at the sidewalls and the saturation of flow velocity observed at the surface. Since the base's roughness is identical in each location, we believe it possible that this reduced friction is associated with the strong acoustic vibrations of the plate, induced by the flow itself.

References

Akaike, H. (1971). *Determination of the number of factors by an extended maximum likelihood principle* (Tech. Rep.). Inst. Statist. Math.

Akaike, H. (1974). A new look at the statistical model identification. *IEEE Transactions on Automatic Control*, *19*(6), 716–723. Retrieved from `https://link.springer.com/content/pdf/10.1007%2F978-1-4612-1694-0.pdf`

Akaike, H. (1978). On the likelihood of a time series model. *Journal of the Royal Statistical Society. Series D (The Statistician)*, *27*(3/4), 217–235. Retrieved from `http://www.jstor.org/stable/2988185`

Allstadt, K. (2013). Extracting source characteristics and dynamics of the August 2010 Mount Meager landslide from broadband seismograms. *Journal of Geophysical Research: Earth Surface*, *118*(3), 1472–1490. Retrieved from `https://agupubs.onlinelibrary.wiley.com/doi/abs/10.1002/jgrf.20110` doi: 10.1002/jgrf.20110

Arran, M. I., Mangeney, A., de Rosny, J., Farin, M., Toussaint, R., & Roche, O. (2020). *Laboratory landquakes* (Vol. (In progress)).

Babic, M. (1997). Average balance equations for granular materials. *International Journal of Engineering Science*, *35*(5), 523–548. Retrieved from `http://www.sciencedirect.com/science/article/pii/S0020722596000948` doi: 10.1016/S0020-7225(96)00094-8

Bachelet, V. (2018). *Étude expérimentale des émissions acoustiques générées par les écoulements granulaires* (Unpublished doctoral dissertation). Institut de Physique du Globe de Paris.

Berrocal, J., Espinosa, A., & Galdos, J. (1978). Seismological and geological aspects of the Mantaro landslide in Peru. *Nature*, *275*, 553–536.

Börzsönyi, T., & Ecke, R. E. (2006, December). Rapid granular flows on a rough

incline: phase diagram, gas transition, and effects of air drag. *Physical Review E*, *74*(6 Pt 1), 061301. Retrieved from `https://doi.org/10.1103/PhysRevE.74.061301` doi: 10.1103/physreve.74.061301

Brodsky, E. E., Gordeev, E., & Kanamori, H. (2003). Landslide basal friction as measured by seismic waves. *Geophysical Research Letters*, *30*(24). Retrieved from `https://agupubs.onlinelibrary.wiley.com/doi/abs/10.1029/2003GL018485` doi: 10.1029/2003GL018485

Capozza, R., Vanossi, A., Vezzani, A., & Zapperi, S. (2009). Suppression of friction by mechanical vibrations. *Physical Review Letters*, *103*, 085502. doi: 10.1103/PhysRevLett.103.085502

Chao, W.-A., Wu, Y.-M., Zhao, L., Chen, H., Chen, Y.-G., Chang, J.-M., & Lin, C.-M. (2017). A first near real-time seismology-based landquake monitoring system. *Scientific Reports*, *7*, 43510. doi: 10.1038/srep43510

Ciarlet, P. G. (1997). Chapter 1 - Linearly Elastic Plates. In P. G. Ciarlet (Ed.), *Mathematical Elasticity* (Vol. 27, pp. 3–127). Elsevier. Retrieved from `http://www.sciencedirect.com/science/article/pii/S0168202497800070` doi: 10.1016/S0168-2024(97)80007-0

Clark, A. H., & Dijksman, J. A. (2020). Editorial: Non-local modeling and diverging lengthscales in structured fluids. *Frontiers in Physics*, *8*, 18. Retrieved from `https://www.frontiersin.org/article/10.3389/fphy.2020.00018` doi: 10.3389/fphy.2020.00018

Coe, J. A., Baum, R. L., Allstadt, K. E., Kochevar, J., Bernard F., Schmitt, R. G., Morgan, M. L., . . . Kean, J. W. (2016). Rock-avalanche dynamics revealed by large-scale field mapping and seismic signals at a highly mobile avalanche in the West Salt Creek valley, western Colorado. *Geosphere*, *12*(2), 607–631. Retrieved from `https://doi.org/10.1130/GES01265.1` doi: 10.1130/GES01265.1

Cuomo, S. (2020). Modelling of flowslides and debris avalanches in natural and engineered slopes: a review. *Geoenvironmental Disasters*, *7*(1).

da Cruz, F., Emam, S., Prochnow, M., Roux, J.-N., & Chevoir, F. (2005). Rheophysics of dense granular materials: Discrete simulation of plane shear flows. *Physical Review E*, *72*, 021309. Retrieved from `https://link.aps.org/doi/10.1103/PhysRevE.72.021309` doi: 10.1103/PhysRevE.72.021309

1005 Dahlen, F. A. (1993). Single-force representation of shallow landslide sources.

1006 *Bulletin of the Seismological Society of America*, *83*(1), 130. Retrieved from

1007 http://dx.doi.org/

1008 Dammeier, F., Moore, J. R., Hammer, C., Haslinger, F., & Loew, S. (2016). Au-

1009 tomatic detection of alpine rockslides in continuous seismic data using hidden

1010 Markov models. *Journal of Geophysical Research: Earth Surface*, *121*(2), 351–

1011 371. Retrieved from https://agupubs.onlinelibrary.wiley.com/doi/abs/

1012 10.1002/2015JF003647 doi: 10.1002/2015JF003647

1013 Dammeier, F., Moore, J. R., Haslinger, F., & Loew, S. (2011). Characterization

1014 of alpine rockslides using statistical analysis of seismic signals. *Journal of Geo-*

1015 *physical Research: Earth Surface*, *116*(F4). Retrieved from https://agupubs

1016 .onlinelibrary.wiley.com/doi/abs/10.1029/2011JF002037 doi: 10.1029/

1017 2011JF002037

1018 Davies, T. R. H. (1982). Spreading of rock avalanche debris by mechanical fluidiza-

1019 tion. *Rock mechanics*, *15*, 9–24.

1020 Delannay, R., Valance, A., Mangeney, A., Roche, O., & Richard, P. (2017). Gran-

1021 ular and particle-laden flows: from laboratory experiments to field obser-

1022 vations. *Journal of Physics D: Applied Physics*, *50*(5), 053001. Retrieved

1023 from https://doi.org/10.1088%2F1361-6463%2F50%2F5%2F053001 doi:

1024 10.1088/1361-6463/50/5/053001

1025 Deparis, J., Jongmans, D., Cotton, F., Baillet, L., Thouvenot, F., & Hantz, D.

1026 (2008). Analysis of rock-fall and rock-fall avalanche seismograms in the

1027 French Alps. *Bulletin of the Seismological Society of America*, *98*(4),

1028 1781–1796. Retrieved from https://doi.org/10.1785/0120070082 doi:

1029 10.1785/0120070082

1030 Dijksman, J. A., Wortel, G. H., van Dellen, L. T. H., Dauchot, O., & van Hecke,

1031 M. (2011). Jamming, yielding, and rheology of weakly vibrated gran-

1032 ular media. *Physical Review Letters*, *107*, 108303. Retrieved from

1033 https://link.aps.org/doi/10.1103/PhysRevLett.107.108303 doi:

1034 10.1103/PhysRevLett.107.108303

1035 Eissler, H., & Kanamori, H. (1987). A single-force model for the 1975 Kalapana,

1036 Hawaii earthquake. *Journal of Geophysical Research*, *92*, 4827–4836. doi: 10

1037 .1029/JB092iB06p04827

1038   Ekström, G., & Stark, C. P.   (2013).   Simple scaling of catastrophic landslide dy-
1039   namics.   *Science*, *339*(6126), 1416–1419.   Retrieved from `http://science`
1040   `.sciencemag.org/content/339/6126/1416`   doi: 10.1126/science.1232887

1041   Farin, M., Mangeney, A., de Rosny, J., Toussaint, R., & Trinh, P.-T.   (2018).
1042   Link between the dynamics of granular flows and the generated seismic
1043   signal: Insights from laboratory experiments.   *Journal of Geophysical*
1044   *Research: Earth Surface*, *123*(6), 1407–1429.   Retrieved from `https://`
1045   `agupubs.onlinelibrary.wiley.com/doi/abs/10.1029/2017JF004296`   doi:
1046   10.1029/2017JF004296

1047   Farin, M., Tsai, V. C., Lamb, M. P., & Allstadt, K. E.   (2019).   A physical
1048   model of the high-frequency seismic signal generated by debris flows.   *Earth*
1049   *Surface Processes and Landforms*, *44*(13), 2529–2543.   Retrieved from
1050   `https://onlinelibrary.wiley.com/doi/abs/10.1002/esp.4677`   doi:
1051   10.1002/esp.4677

1052   Favreau, P., Mangeney, A., Lucas, A., Crosta, G., & Bouchut, F.   (2010).   Numerical
1053   modeling of landquakes.   *Geophysical Research Letters*, *37*(15).   Retrieved
1054   from `https://agupubs.onlinelibrary.wiley.com/doi/abs/10.1029/`
1055   `2010GL043512`   doi: 10.1029/2010GL043512

1056   Ferdowsi, B., Griffa, M., Guyer, R., Johnson, P., & Carmeliet, J.   (2014).   Effect
1057   of boundary vibration on the frictional behavior of a dense sheared granular
1058   layer. *Acta Mechanica*, *225*, 2227–2237.

1059   Fleming, R., Taylor, F., & (U.S.), G. S.   (1980).   *Estimating the costs of landslide*
1060   *damage in the United States.*   U.S. Department of the Interior, Geological Sur-
1061   vey. Retrieved from `https://books.google.fr/books?id=DGnlhwP6h8cC`

1062   Froude, M. J., & Petley, D. N.   (2018).   Global fatal landslide occurrence from 2004
1063   to 2016. *Nat. Hazards Earth Syst. Sci.*, *18*, 2161–2181.

1064   Fuchs, F., Lenhardt, W., Bokelmann, G., & the AlpArray Working Group.   (2018).
1065   Seismic detection of rockslides at regional scale: examples from the Eastern
1066   Alps and feasibility of kurtosis-based event location.   *Earth Surface Dynamics*,
1067   *6*. doi: 10.5194/esurf-6-955-2018

1068   Fukao, Y. (1995). Single-force representation of earthquakes due to landslides or the
1069   collapse of caverns.   *Geophysical Journal International*, *122*(1), 243–248.   Re-
1070   trieved from `https://doi.org/10.1111/j.1365-246X.1995.tb03551.x`   doi:

1071   10.1111/j.1365-246X.1995.tb03551.x

1072 Galitzine (Golitsyn), B.   (1915).   Sur le tremblement de terre du 18 février 1911.

1073   *Comptes rendus hebdomadaires des séances de l'Académie des sciences*, *160*,

1074   810–813.

1075 Garve, T. W. (1925). Segregation in bins. *J. Amer. Ceram. Soc.*, *80*, 666.

1076 GDR MiDi.   (2004, 01).   On dense granular flows.   *The European Physical Jour-

1077   nal E*, *14*(4), 341–365.   Retrieved from `https://doi.org/10.1140/epje/`

1078   `i2003-10153-0`   doi: 10.1140/epje/i2003-10153-0

1079 Gimbert, F., & Tsai, V. C.   (2015).   Predicting short-period, wind-wave-generated

1080   seismic noise in coastal regions.   *Earth and Planetary Science Letters*, *426*,

1081   280–292. Retrieved from `http://www.sciencedirect.com/science/article/`

1082   `pii/S0012821X15003738`   doi: 10.1016/j.epsl.2015.06.017

1083 Given, D. D., Allen, R. M., Baltay, A. S., Bodin, P., Cochran, E. S., Creager, K., . . .

1084   Yelin, T. S.   (2018).   *Revised technical implementation plan for the ShakeAl-

1085   ert system: An earthquake early warning system for the West Coast of the

1086   United States* (Tech. Rep.).   U.S. Geological Survey Open-File Report.   doi:

1087   10.3133/ofr20181155

1088 Goldhirsch, I.   (2003).   Rapid granular flows.   *Annual Review of Fluid Mechanics*,

1089   *35*(1), 267–293.   Retrieved from `https://doi.org/10.1146/annurev.fluid`

1090   `.35.101101.161114`   doi: 10.1146/annurev.fluid.35.101101.161114

1091 Gollin, D., Berzi, D., & Bowman, E.   (2017).   Extended kinetic theory applied to in-

1092   clined granular flows: role of boundaries. *Granular Matter*, *19*(56).

1093 Gray, J. M. N. T. (2018). Particle Segregation in Dense Granular Flows. *Annual Re-

1094   view of Fluid Mechanics*, *50*(1), 407–433.   Retrieved from `https://doi.org/`

1095   `10.1146/annurev-fluid-122316-045201`   doi: 10.1146/annurev-fluid-122316

1096   -045201

1097 Guzzetti, F., Gariano, S. L., Peruccacci, S., Brunetti, M. T., Marchesini, I.,

1098   Rossi, M., & Melillo, M.   (2020).   Geographical landslide early warn-

1099   ing systems.   *Earth-Science Reviews*, *200*, 102973.   Retrieved from

1100   `http://www.sciencedirect.com/science/article/pii/S0012825219304635`

1101   doi: 10.1016/j.earscirev.2019.102973

1102 Hanes, D. M., & Walton, O. R.   (2000).   Simulations and physical measurements of

1103   glass spheres flowing down a bumpy incline.   *Powder Technology*, *109*(1), 133–

144. Retrieved from `http://www.sciencedirect.com/science/article/pii/` `S0032591099002326` doi: 10.1016/S0032-5910(99)00232-6

Hasegawa, H. S., & Kanamori, H. (1987). Source mechanism of the magnitude 7.2 Grand Banks earthquake of November 1929: Double couple or submarine landslide? *Bulletin of the Seismological Society of America*, *77*(6), 1984. Retrieved from `http://dx.doi.org/`

Hertz, H. R. (1881). Über die berührung fester elastischer körper. *Journal für die reine und angewandte Mathematik*, *92*, 156–171. Retrieved from `https://home` `.uni-leipzig.de/pwm/web/download/Hertz1881.pdf`

Hervás, J. E. (2003). *Lessons learnt from landslide disasters in Europe. eur 20558 en* (Tech. Rep.). Ispra, Italy: European Commission.

Hibert, C., Ekström, G., & Stark, C. P. (2017). The relationship between bulk-mass momentum and short-period seismic radiation in catastrophic landslides. *Journal of Geophysical Research: Earth Surface*, *122*(5), 1201–1215. Retrieved from `https://agupubs.onlinelibrary.wiley.com/doi/abs/10.1002/` `2016JF004027` doi: 10.1002/2016JF004027

Hibert, C., Mangeney, A., Grandjean, G., Baillard, C., Rivet, D., Shapiro, N. M., . . . Crawford, W. (2014). Automated identification, location, and volume estimation of rockfalls at Piton de la Fournaise volcano. *Journal of Geophysical Research: Earth Surface*, *119*(5), 1082–1105. Retrieved from `https://` `agupubs.onlinelibrary.wiley.com/doi/abs/10.1002/2013JF002970` doi: 10.1002/2013JF002970

Hibert, C., Mangeney, A., Grandjean, G., & Shapiro, N. M. (2011). Slope instabilities in Dolomieu crater, Réunion Island: From seismic signals to rockfall characteristics. *Journal of Geophysical Research: Earth Surface*, *116*(F4). doi: 10.1029/2011JF002038

Hibert, C., Stark, C. P., & Ekström, G. (2015). Dynamics of the Oso-Steelhead landslide from broadband seismic analysis. *Natural Hazards and Earth System Sciences*, *15*(6), 1265–1273. Retrieved from `https://www.nat-hazards-earth` `-syst-sci.net/15/1265/2015/` doi: 10.5194/nhess-15-1265-2015

Hsu, L., Dietrich, W. E., & Sklar, L. S. (2014). Mean and fluctuating basal forces generated by granular flows: Laboratory observations in a large vertically rotating drum. *Journal of Geophysical Research: Earth Surface*, *119*(6), 1283–

1309. Retrieved from `https://agupubs.onlinelibrary.wiley.com/doi/abs/`
`10.1002/2013JF003078` doi: 10.1002/2013JF003078

Hungr, O., & Morgenstern, N. R. (1984). Experiments on the flow behaviour of
granular materials at high velocity in an open channel. *Géotechnique*, *34*(3),
405–413. Retrieved from `https://doi.org/10.1680/geot.1984.34.3.405`
doi: 10.1680/geot.1984.34.3.405

Hurvich, C. M., & Tsai, C.-L. (1989). Regression and time series model selection in
small samples. *Biometrika*, *76*(2), 297–307. Retrieved from `https://doi.org/`
`10.1093/biomet/76.2.297` doi: 10.1093/biomet/76.2.297

Jeffreys, H. (1923). The Pamir earthquake of 1911 February 18, in relation to the
depths of earthquake foci. *Geophysical Journal International*, *1*(s2), 22–31.
Retrieved from `https://onlinelibrary.wiley.com/doi/abs/10.1111/`
`j.1365-246X.1923.tb06566.x` doi: 10.1111/j.1365-246X.1923.tb06566.x

Jing, L., Kwok, C. Y., Leung, Y. F., & Sobral, Y. D. (2016). Characterization of
base roughness for granular chute flows. *Physical Review E*, *94*, 052901. Re-
trieved from `https://link.aps.org/doi/10.1103/PhysRevE.94.052901` doi:
10.1103/PhysRevE.94.052901

John Steel. (2019). *Fiche technique acier s355* (Tech. Rep.). Author. Retrieved
from `https://www.john-steel.com/fr/acier/29-plaque-d-acier-decape`
`-et-graisse.html`

Johnson, P. A., Savage, H., Knuth, M., Gomberg, J., & Marone, C. (2008). Ef-
fects of acoustic waves on stick–slip in granular media and implications for
earthquakes. *Nature*, *451*, 57–60.

Jop, P., Forterre, Y., & Pouliquen, O. (2005). Crucial role of sidewalls in granular
surface flows: consequences for the rheology. *Journal of Fluid Mechanics*, *541*,
167–192. doi: 10.1017/S0022112005005987

Jop, P., Forterre, Y., & Pouliquen, O. (2006). A constitutive law for dense granular
flows. *Nature*, *441*(7094), 727–730. Retrieved from `http://www.nature`
`.com/nature/journal/v441/n7094/suppinfo/nature04801\_S1.html`
(10.1038/nature04801) doi: 10.1038/nature04801

Kanamori, H., & Given, J. W. (1982). Analysis of long-period seismic waves excited
by the May 18, 1980, eruption of Mount St. Helens - A terrestrial monopole?
Journal of Geophysical Research: Solid Earth, *87*(B7), 5422–5432. Retrieved

1170   from `https://agupubs.onlinelibrary.wiley.com/doi/abs/10.1029/`

1171   `JB087iB07p05422` doi: 10.1029/JB087iB07p05422

1172 Kawakatsu, H. (1989). Centroid single force inversion of seismic waves generated

1173   by landslides. *Journal of Geophysical Research: Solid Earth*, *94*(B9), 12363–

1174   12374. Retrieved from `https://agupubs.onlinelibrary.wiley.com/doi/`

1175   `abs/10.1029/JB094iB09p12363` doi: 10.1029/JB094iB09p12363

1176 Kean, J. W., Coe, J. A., Coviello, V., Smith, J. B., McCoy, S. W., & Arattano, M.

1177   (2015). Estimating rates of debris flow entrainment from ground vibrations.

1178   *Geophysical Research Letters*, *42*(15), 6365–6372. Retrieved from `https://`

1179   `agupubs.onlinelibrary.wiley.com/doi/abs/10.1002/2015GL064811` doi:

1180   10.1002/2015GL064811

1181 Kim, D. H., Gratchev, I., Berends, J., & Balasubramaniam, A. (2015). Calibration

1182   of restitution coefficients using rockfall simulations based on 3d photogram-

1183   metry model: a case study. *Natural Hazards*, *78*, 1931–1946. Retrieved from

1184   `https://doi.org/10.1007/s11069-015-1811-x`

1185 Kullback, S., & Leibler, R. A. (1951). On information and sufficiency. *Ann. Math.*

1186   *Statist.*, *22*(1), 79–86. Retrieved from `https://doi.org/10.1214/aoms/`

1187   `1177729694` doi: 10.1214/aoms/1177729694

1188 La Rocca, M., Galluzzo, D., Saccorotti, G., Tinti, S., Cimini, G. B., & Del Pezzo,

1189   E. (2004). Seismic signals associated with landslides and with a tsunami at

1190   Stromboli volcano, Italy. *Bulletin of the Seismological Society of America*,

1191   *94*(5), 1850–1867. Retrieved from `https://doi.org/10.1785/012003238` doi:

1192   10.1785/012003238

1193 Lai, V. H., Tsai, V. C., Lamb, M. P., Ulizio, T. P., & Beer, A. R. (2018). The

1194   seismic signature of debris flows: Flow mechanics and early warning at Mon-

1195   tecito, California. *Geophysical Research Letters*, *45*(11), p5528–5535. doi:

1196   10.1029/2018GL077683

1197 Lastakowski, H., Géminard, J.-C., & Vidal, V. (2015). Granular friction: Triggering

1198   large events with small vibrations. *Scientific Reports*, *5*, 13455.

1199 Lee, E.-J., Liao, W.-Y., Lin, G.-W., Chen, P., Mu, D., & Lin, C.-W. (2019). To-

1200   wards automated real-time detection and location of large-scale landslides

1201   through seismic waveform back projection. *Geofluids*. doi: 10.1155/2019/

1202   1426019

1203 Lemrich, L., Carmeliet, J., Johnson, P. A., Guyer, R., & Jia, X. (2017). Dynamic
1204 induced softening in frictional granular materials investigated by discrete-
1205 element-method simulation. *Physical Review E*, *96*, 062901. Retrieved
1206 from https://link.aps.org/doi/10.1103/PhysRevE.96.062901 doi:
1207 10.1103/PhysRevE.96.062901

1208 Levy, C., Mangeney, A., Bonilla, F., Hibert, C., Calder, E. S., & Smith, P. J. (2015).
1209 Friction weakening in granular flows deduced from seismic records at the
1210 Soufrière Hills volcano, Montserrat. *Journal of Geophysical Research: Solid*
1211 *Earth*, *120*(11), 7536–7557. Retrieved from https://agupubs.onlinelibrary
1212 .wiley.com/doi/abs/10.1002/2015JB012151 doi: 10.1002/2015JB012151

1213 Lin, C.-H., Kumagai, H., Ando, M., & Shin, T. (2010). Detection of landslides and
1214 submarine slumps using broadband seismic networks. *Geophysical Research*
1215 *Letters*, *37*. doi: 10.1029/2010GL044685

1216 Love, A. E. H., & Darwin, G. H. (1888). XVI. the small free vibrations and
1217 deformation of a thin elastic shell. *Philosophical Transactions of the*
1218 *Royal Society of London. (A.)*, *179*, 491–546. Retrieved from https://
1219 royalsocietypublishing.org/doi/abs/10.1098/rsta.1888.0016 doi:
1220 10.1098/rsta.1888.0016

1221 Lucas, A., Mangeney, A., & Ampuero, J. P. (2014). Frictional velocity-weakening
1222 in landslides on Earth and on other planetary bodies. *Nature Communications*,
1223 *5*, 3417. doi: 10.1038/ncomms4417

1224 McCoy, S. W., Tucker, G. E., Kean, J. W., & Coe, J. A. (2013). Field mea-
1225 surement of basal forces generated by erosive debris flows. *Journal of*
1226 *Geophysical Research: Earth Surface*, *118*(2), 589–602. Retrieved from
1227 https://agupubs.onlinelibrary.wiley.com/doi/abs/10.1002/jgrf.20041
1228 doi: 10.1002/jgrf.20041

1229 McLaskey, G. C., & Glaser, S. D. (2010). Hertzian impact: Experimental study of
1230 the force pulse and resulting stress waves. *The Journal of the Acoustical Soci-*
1231 *ety of America*, *128*(3), 1087–1096. Retrieved from https://asa.scitation
1232 .org/doi/abs/10.1121/1.3466847 doi: 10.1121/1.3466847

1233 Michlmayr, G., & Or, D. (2014, 01). Mechanisms for acoustic emissions gener-
1234 ation during granular shearing. *Granular Matter*, *16*(5), 627–640. Re-
1235 trieved from https://doi.org/10.1007/s10035-014-0516-2 doi:

1236   10.1007/s10035-014-0516-2

1237 Miller, G. F., & Pursey, H. (1954). The Field and Radiation Impedance of
1238   Mechanical Radiators on the Free Surface of a Semi-Infinite Isotropic
1239   Solid. *Proceedings of the Royal Society of London A: Mathematical,*
1240   *Physical and Engineering Sciences*, *223*(1155), 521–541. Retrieved from
1241   `http://rspa.royalsocietypublishing.org/content/223/1155/521` doi:
1242   10.1098/rspa.1954.0134

1243 Moretti, L., Allstadt, K., Mangeney, A., Capdeville, Y., Stutzmann, E., & Bouchut,
1244   F. (2015). Numerical modeling of the Mount Meager landslide con-
1245   strained by its force history derived from seismic data. *Journal of Geophys-*
1246   *ical Research: Solid Earth*, *120*(4), 2579–2599. Retrieved from `https://`
1247   `agupubs.onlinelibrary.wiley.com/doi/abs/10.1002/2014JB011426` doi:
1248   10.1002/2014JB011426

1249 Moretti, L., Mangeney, A., Capdeville, Y., Stutzmann, E., Huggel, C., Schneider, D.,
1250   & Bouchut, F. (2012). Numerical modeling of the Mount Steller landslide flow
1251   history and of the generated long period seismic waves. *Geophysical Research*
1252   *Letters*, *39*(16). Retrieved from `https://agupubs.onlinelibrary.wiley`
1253   `.com/doi/abs/10.1029/2012GL052511` doi: 10.1029/2012GL052511

1254 Moretti, L., Mangeney, A., Walter, F., Capdeville, Y., Bodin, T., Stutzmann, E.,
1255   & Le Friant, A. (2020). Constraining landslide characteristics with Bayesian
1256   inversion of field and seismic data. *Geophysical Journal International*. Re-
1257   trieved from `https://doi.org/10.1093/gji/ggaa056` (ggaa056) doi:
1258   10.1093/gji/ggaa056

1259 National Research Council. (1985). *Reducing losses from landsliding in the united*
1260   *states.* The National Academies Press.

1261 Nishiguchi, Y., Uchida, T., Takezawa, N., Ishizuka, T., & Mizuyama, T. (2012).
1262   Runout characteristics and grain size distribution of large-scale debris flows
1263   triggered by deep catastrophic landslides. *International Journal of Erosion*
1264   *Control Engineering*, *5*(1), 16–26. doi: 10.13101/ijece.5.16

1265 Norris, R. D. (1994). Seismicity of rockfalls and avalanches at three Cascade range
1266   volcanoes: Implications for seismic detection of hazardous mass movements.
1267   *Bulletin of the Seismological Society of America*, *84*(6), 1925. Retrieved from
1268   `http://dx.doi.org/`

1269 Peterschmitt, É., & de Visintini, G.   (1964).   Sur les enregistrements séismiques as-
1270   sociés à la catastrophe de la digue de Vajont du 9 octobre 1963.   *Comptes ren-*
1271   *dus hebdomadaires des séances de l'Académie des sciences*, *258*, 2629–2632.

1272 Plancherel, M., & Mittag-Leffler, G.   (1910).   Contribution à l'étude de la
1273   représentation d'une fonction arbitraire par les intégrales définies.   *Rendiconti*
1274   *del Circolo Matematico di Palermo*, *30*(1), 289–335.

1275 Pudasaini, S., & Hutter, K. (2006). *Avalanche dynamics: Dynamics of rapid flows of*
1276   *dense granular avalanches.*   Springer.   Retrieved from `https://books.google`
1277   `.co.uk/books?id=gri6NAEACAAJ`

1278 Roche, O., van den Wildenberg, S., Valance, A., Delannay, R., Mangeney, A., Corna,
1279   L., & Latchimy, T.   (2020).   Measurement of effective friction at the base of
1280   granular flows in an inclined channel. *Physical Review E*, *(Under review)*.

1281 Schneider, D., Bartelt, P., Caplan-Auerbach, J., Christen, M., Huggel, C., &
1282   McArdell, B. W.   (2010).   Insights into rock-ice avalanche dynamics by com-
1283   bined analysis of seismic recordings and a numerical avalanche model.   *Journal*
1284   *of Geophysical Research: Earth Surface*, *115*(F4).   Retrieved from `https://`
1285   `agupubs.onlinelibrary.wiley.com/doi/abs/10.1029/2010JF001734`   doi:
1286   10.1029/2010JF001734

1287 Scholl, H. J., Ballard, S., Carnes, S., Herman, A., & Parker, N.   (2017).   Informa-
1288   tional challenges in early disaster response: The massive Oso/SR530 landslide
1289   2014 as case in point.   *Proceedings of the 50th Hawaii International Conference*
1290   *on System Sciences*.

1291 Schuster, R. L., & Fleming, R. W.   (1986).   Economic losses and fatalities due to
1292   landslides.   *Bulletin of the Association of Engineering Geologists*, *23*(1), p11–
1293   28.

1294 Sigmund Lindner.   (2018).   *Product data sheet.*   Retrieved online.   Retrieved
1295   from `https://www.sigmund-lindner.com/en/products/glass-beads/`
1296   `dispersing-beads/`

1297 Silbert, L. E., Ertaş, D., Grest, G. S., Halsey, T. C., Levine, D., & Plimpton, S. J.
1298   (2001).   Granular flow down an inclined plane: Bagnold scaling and rheology.
1299   *Physical Review E*, *64*, 051302.   Retrieved from `https://link.aps.org/doi/`
1300   `10.1103/PhysRevE.64.051302`   doi: 10.1103/PhysRevE.64.051302

1301 Steel SS. (2019). *Data table for carbon steel s355mc* (Tech. Rep.). Author. Retrieved

1302   from `https://www.steelss.com/Carbon-steel/s355mc.html`

1303   Suriñach, E., Vilajosana, I., Khazaradze, G., Biescas, B., Furdada, G., & Vilaplana,

1304   J. M. (2005). Seismic detection and characterization of landslides and other

1305   mass movements. *Natural Hazards and Earth System Sciences*, *5*(6), 791–798.

1306   Retrieved from `https://www.nat-hazards-earth-syst-sci.net/5/791/`

1307   `2005/` doi: 10.5194/nhess-5-791-2005

1308   Taberlet, N., Richard, P., Jenkins, J. T., & Delannay, R. (2007). Density inversion in

1309   rapid granular flows: the supported regime. *Eur. Phys. J. E*, *22*(1), 17–24. Re-

1310   trieved from `https://doi.org/10.1140/epje/e2007-00010-5` doi: 10.1140/

1311   epje/e2007-00010-5

1312   Takahashi, T. (1981). Debris flow. *Annual Review of Fluid Mechanics*, *13*(1), 57–77.

1313   Retrieved from `https://doi.org/10.1146/annurev.fl.13.010181.000421`

1314   doi: 10.1146/annurev.fl.13.010181.000421

1315   Taylor, S., & Brodsky, E. E. (2017). Granular temperature measured experimen-

1316   tally in a shear flow by acoustic energy. *Physical Review E*, *96*, 032913. Re-

1317   trieved from `https://link.aps.org/doi/10.1103/PhysRevE.96.032913` doi:

1318   10.1103/PhysRevE.96.032913

1319   Tsai, V. C., & Atiganyanun, S. (2014). Green's functions for surface waves in a

1320   generic velocity structure. *Bulletin of the Seismological Society of America*,

1321   *104*(5), 2573–2578. Retrieved from `https://doi.org/10.1785/0120140121`

1322   doi: 10.1785/0120140121

1323   Tsai, V. C., Minchew, B., Lamb, M. P., & Ampuero, J.-P. (2012). A physical model

1324   for seismic noise generation from sediment transport in rivers. *Geophysical*

1325   *Research Letters*, *39*(2). Retrieved from `https://agupubs.onlinelibrary`

1326   `.wiley.com/doi/abs/10.1029/2011GL050255` doi: 10.1029/2011GL050255

1327   Tsang, J. M. F., Dalziel, S. B., & Vriend, N. M. (2019). The granular Blasius prob-

1328   lem. *Journal of Fluid Mechanics*, *872*, 784–817. doi: 10.1017/jfm.2019.357

1329   van Asch, T., Malet, J., van Beek, L., & Amitrano, D. (2007). Techniques, advances,

1330   problems and issues in numerical modelling of landslide hazard. *Bulletin de la*

1331   *Société Géologique de France*, *178*(2), p65–88.

1332   Weichert, D., Horner, R. B., & Evans, S. G. (1994). Seismic signatures of landslides:

1333   The 1990 Brenda Mine collapse and the 1965 Hope rockslides. *Bulletin of the*

1334   *Seismological Society of America*, *84*(5), 1523–1532.

Yamada, M., Kumagai, H., Matsushi, Y., & Matsuzawa, T. (2013). Dynamic landslide processes revealed by broadband seismic records. *Geophysical Research Letters*, *40*(12), 2998–3002. Retrieved from https://agupubs.onlinelibrary.wiley.com/doi/abs/10.1002/grl.50437 doi: 10.1002/grl.50437

Yamada, M., Mangeney, A., Matsushi, Y., & Matsuzawa, T. (2018). Estimation of dynamic friction and movement history of large landslides. *Landslides*, *15*, 1963–1974. doi: 10.1007/s10346-018-1002-4

Yamada, M., Mangeney, A., Matsushi, Y., & Moretti, L. (2016). Estimation of dynamic friction of the Akatani landslide from seismic waveform inversion and numerical simulation. *Geophysical Journal International*, *206*(3), 1479–1486. Retrieved from https://doi.org/10.1093/gji/ggw216 doi: 10.1093/gji/ggw216

Zhao, J., Ouyang, C. J., Ni, S. D., Chu, R. S., & Mangeney, A. (2020). Analysis of the June 2017 Maoxian Landslide Processes with Force Histories from Seismological Inversion and Terrain Features. *Geophysical Journal International*. Retrieved from https://doi.org/10.1093/gji/ggaa269 (ggaa269) doi: 10.1093/gji/ggaa269